Modelling Simul. Mater. Sci. Eng. **17** (2009) 073001 (31pp) doi:10.1088/0965-0393/17/7/073001

TOPICAL REVIEW

Phase-field models in materials science

Ingo Steinbach

Interdisciplinary Centre for Advanced Materials Simulation (ICAMS), Ruhr-University Bochum Germany

E-mail: ingo.steinbach@rub.de

Received 22 September 2008, in final form 8 June 2009
Published 30 July 2009
Online at stacks.iop.org/MSMSE/17/073001

Abstract
The phase-field method is reviewed against its historical and theoretical background. Starting from Van der Waals considerations on the structure of interfaces in materials the concept of the phase-field method is developed along historical lines. Basic relations are summarized in a comprehensive way. Special emphasis is given to the multi-phase-field method with extension to elastic interactions and fluid flow which allows one to treat multi-grain multi-phase structures in multicomponent materials. Examples are collected demonstrating the applicability of the different variants of the phase-field method in different fields of materials science.

1. Introduction

'The phase-field approach has emerged as a method of choice to simulate microstructure evolution during solidification', is how the seminal paper of Alain Karma about dendritic alloy solidification starts, which marks a breakthrough towards quantitative simulation [1]. Today we can broaden the range of application from solidification to 'microstructure evolution in materials processing' with a wide range of materials and processes, including microstructural evolution during life time and service. Thereby the level of sophistication competes with the level of quantitativeness because, particularly in solid state, the mechanisms of transformation are sometimes not as clear as in solidification and the model formulation becomes difficult. Nevertheless, today quantitative methods developed in solidification are also used in solid state and the interest in predictive calculations increasingly supersedes the purely qualitative demonstration of effects. An exhaustive review of the field is nearly impossible due to the broad range of applications. Nevertheless a number of excellent reviews which shed light on the subject from different standpoints are available [2–7]. This review aims to give a tutorial compilation of the underlying physical ideas and mathematical formulations with explanations that also make the mathematics comprehensible for non-experts. The focus will lie on the multi-phase-field (MPF) method as developed by the author. New material, which can help one to

understand some of the hidden know-how behind published information, is added. Examples are collected to illustrate different aspects of phase-field modeling. Let us start with a historical view.

2. Historical background

The principal characteristic of phase-field models is the diffuseness of the interface between two phases, which are sometimes also called 'diffuse interface models'. The interface is described by a steep, but continuous, transition (in real space $\vec{x}$) of the phase field variable $\phi(\vec{x}, t)$ between two states. This view of a 'diffuse interface' dates back to van der Waals [8], who analyzed the forces between atoms and molecules. From general thermodynamic considerations he rationalized that a diffuse interface between stable phases of a material is more natural than the assumption of a sharp interface with a discontinuity in at least one property of the material[1]. A second characteristic of phase-field models is that non-equilibrium states are addressed in general. The phase field variable distinguishes between different states of a material that may be identical in all other state variables such as temperature, concentration, pressure, etc. Therefore, the phase-field variable is an independent state variable. In their famous theory of phase transitions Ginzburg and Landau [9] used this observation to expand the thermodynamic state functions, which they called 'order parameter', and its gradients. Hillert developed the first model for spinodal decomposition, where the order parameter was used as a (discrete) field variable in space and time [10]. Cahn and Hilliard treated the same problem in a continuous way and used the alloy concentration as the order parameter [11, 12]. All these early models considered the diffusiveness of the interface as real and a property of the interface that can be predicted from the thermodynamic functional. I will, however, adopt the pragmatic view following Langer [13], that the diffuseness of the phase field exists on a scale that is below the microstructure scale of interest. Thus its thickness can be set to a value that is appropriate for a numerical simulation. Reference shall also be given to Khachaturyan's theory of micro-elasticity [14] that created the basis for a whole school of phase-field models mainly applied to microstructure evolution in solid state (see [4, 15–18, 20]). I want to start this review with Kobayashi's dendrite.

2.1. Kobayashi's dendrite

The first time I came into contact with 'phase field' was at the 1993 McWasp conference in Palm Coast, Florida (Modeling of Casting, Welding and Advanced Solidification Processes VII) where Bill Boettinger presented a poster [21] with the newly developed alloy solidification model (section 2.2) and where the growing of Kobayashi's dendrite was displayed on a video screen. Ryo Kobayashi had developed a scheme to solve Stefan's problem of solidification of a pure substance in an undercooled melt by replacing the sharp interface moving boundary problem by a diffuse interface scheme [22, 23]. This scheme has a striking simplicity and turned out to be identical to the theoretical concepts we nowadays call phase field. The scheme consists of two partial differential equations, the diffusion equation for the temperature field $T(\vec{x}, t)$ and the evolution equation of an indicator function, the phase field $\phi(\vec{x}, t)$ that distinguishes the phases. $\phi = 1$ indicates the solid, $\phi = 0$ the liquid and a smooth transition of $\phi(\vec{x}, t)$ between 1 and 0 indicates the solid–liquid interface. In Kobayashi's notation the phase-field

[1] He examined the density change between a liquid and its vapour.

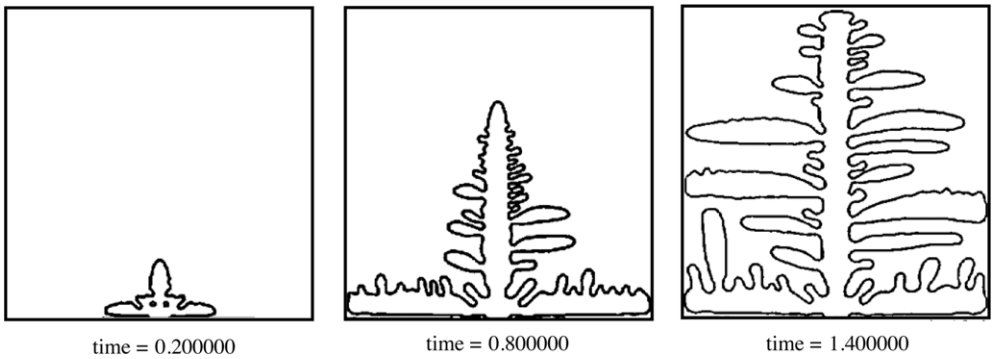

Figure 1. 2D simulation of dendritic growth of a pure substance in a highly undercooled melt, starting from a small seed at the bottom of the domain. Reproduced with permission from [22], © Elsevier 1993.

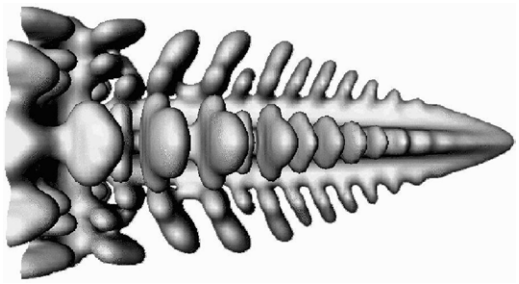

Figure 2. 3D simulation of dendritic growth of a pure substance in a highly undercooled melt. Reproduced with permission from [23], © Elsevier 1994.

equation and the temperature equation read

$$\tau\dot{\phi} = \epsilon\nabla^2\phi + \gamma\phi(1-\phi)\left(\phi - \tfrac{1}{2} + m_0(T_\mathrm{m} - T)\right), \tag{1}$$

$$\dot{T} = \nabla(\lambda_T \nabla T) + \frac{L}{c_p}\dot{\phi}, \tag{2}$$

where τ is a relaxation constant setting the time scale, ϵ and γ are proportional to the interfacial energy that will in general depend on the interface orientation with respect to the orientation of the crystal (see section 3.2), T_m is the equilibrium temperature between solid and liquid of a pure substance (melting temperature). m_0 is proportional to the enthalpy of fusion L. λ_T is the thermal diffusivity and c_p the heat capacity. These two equations are simple parabolic differential equations from their structure. However, both equations are closely coupled. $\dot{\phi}$ in equation (1) depends on the temperature T and $\dot{T}$ in equation (2) depends on $\dot{\phi}$. The system of equations thus becomes highly nonlinear. It is this coupling that will produce the unexpected self-organizing patterns, which correspond to dendritic patterns found in nature. Additionally, the role of interface energy on the mode selection in dendritic growth is reflected by the equations. Figure 1 shows three time steps of a calculated dendritic structure in 2D. The first 3D dendritic structures (figure 2) that show striking similarity to real structures could already be calculated in 1994. Only the scale selection could not yet be controlled by the first schemes (see section 3.3).

Furthermore, it can be seen that equations (1) and (2) are derived from a thermodynamic functional using relaxational dynamics [24]. In this specific case, we are seeking an equation

that is compatible with the principle of entropy maximization, appropriate for adiabatic systems with temperature variations as derived by Wang *et al* [25]. The entropy functional S is defined by the integral of the entropy density s over the domain Ω. It is related to the internal energy density e and the free energy density f in the notation of (1) and (2)

$$S = \int_\Omega s = \int_\Omega \frac{e-f}{T}, \tag{3}$$

$$e = c_p T + L(1-\phi), \tag{4}$$

$$f = \frac{1}{2}\epsilon(\nabla\phi)^2 + \frac{\gamma}{4}\phi^2(1-\phi)^2 - L\frac{T_\mathrm{m}-T}{T_\mathrm{m}}6\left(\frac{\phi^2}{2} - \frac{\phi^3}{3}\right). \tag{5}$$

Here, for simplicity the internal energy of the solid is assumed to be linearly dependent on T with constant specific heat c_p. The governing equations for T and ϕ are derived consistently with the principle of entropy production $\dot{S} > 0$ as explained in detail in [25]

$$\tilde{\tau}\dot{\phi} = -\frac{\delta}{\delta\phi}\left(\int_\Omega \frac{f}{T}\right)_T = -\frac{1}{T}\left[\frac{\partial f}{\partial\phi} - \nabla\frac{\partial f}{\partial\nabla\phi}\right], \tag{6}$$

$$\dot{e} = -\nabla M_T \nabla\frac{\delta}{\delta e}\left(\int_\Omega \frac{e}{T}\right)_\phi = -\nabla\left[M_T\nabla\frac{1}{T}\right]. \tag{7}$$

Inserting the energy model (4) into (7) we obtain the heat conduction equation

$$\dot{e} = c_p\dot{T} - L\dot{\phi} = \nabla\frac{M_T}{T^2}\nabla T, \tag{8}$$

which is equivalent to equation (2) with $\lambda_T = M_T/c_pT^2$. The phase-field equation (1) also follows directly from (6) inserting the free energy model (5) with $\tau = T\tilde{\tau}$ and $6(L/T_\mathrm{m}) = \gamma m_0$.[2]

$$\tilde{\tau}\dot{\phi} = \frac{1}{T}\left[\epsilon\nabla^2\phi - \gamma\phi(1-\phi)\left(\frac{1}{2}-\phi\right) + 6L\frac{T_\mathrm{m}-T}{T_\mathrm{m}}\phi(1-\phi)\right]. \tag{9}$$

The thermodynamically consistent derivation of phase-field models is of special importance, because it enables the correlation of the model parameters with each other, as well as the establishment of a sound theoretical background in thermodynamics.

To conclude this section the special form of the free energy density given in (5) shall be discussed. The first term is the gradient energy contribution which is the only non local contribution in the functional. It is sensitive to variations in the phase-field variable, i.e. to interfaces. The second term is the famous double well potential $f_\mathrm{DW} = \gamma\phi^2(1-\phi)^2$ that sets the minima of the free energy at $\phi = 0$ and $\phi = 1$ with an activation barrier of height $\gamma/16$. Both terms, the gradient and the potential term, contribute in equal parts to the interface energy, as is shown in the appendix. The last term in equation (5) proportional to L shifts the energy minimum at $\phi = 1$ up or down depending on the deviation of the interface temperature from the melting temperature $T - T_\mathrm{m}$. For $T = T_\mathrm{m}$ both phases have the same free energy and (besides curvature driven melting) no phase change will occur. Any deviation of the temperature from the melting temperature will favour either the solid or the liquid. However, the temperature in our problem is not constant but depends on the evolution of ϕ via the last term $L\dot{\phi}$ in (2). This makes the problem so interesting.

[2] One has to apply the standard rules of differentiation for the partial derivatives of the functionals with respect to the field variables. $\nabla\phi$ in (6) is to be used as a single variable.

2.2. The WBM model of alloy solidification

The next step towards application of phase-field models in materials science was the alloy solidification model by Wheeler, Boettinger and McFadden in 1993. They combined the Cahn–Hilliard model for spinodal decomposition and early phase-field models by Langer [13], Collins and Levine [26], Caginalp [27] and Kobayashi [22]. Their basic approach is to construct a generalized free energy functional that depends on both concentration and phase by superposition of two single-phase free energies and weighting them by the alloy concentration. The free energy density equivalent to equation (5) for a binary alloy with concentration c of atoms A and $(1-c)$ of atoms B reads

$$f = \frac{1}{2}\epsilon(\nabla\phi)^2 + cf_{\mathrm{DW}}^{\mathrm{A}} + (1-c)f_{\mathrm{DW}}^{\mathrm{B}} - m^{\mathrm{AB}}(c,T)\left(\frac{\phi^2}{2} - \frac{\phi^3}{3}\right) + \frac{RT}{v_{\mathrm{m}}}[c\ln c + (1-c)\ln(1-c)] \tag{10}$$

$$f_{\mathrm{DW}}^{\mathrm{A/B}} = \gamma^{\mathrm{A/B}}\phi^2(1-\phi)^2, \tag{11}$$

where $f_{\mathrm{DW}}^{\mathrm{A/B}}$ are the potentials of the pure crystals A and B, respectively, v_{m} the molar volume and R the gas constant. The whole potential is now a function of both ϕ and c and reduces to that of a pure substance for $c = 0$ and $c = 1$. It has the same form as for pure systems but contains the concentration-dependent parameters. By comparing it to (5) we can define $\gamma^{\mathrm{AB}}(c) = 4[c\gamma^{\mathrm{A}} + (1-c)\gamma^{\mathrm{B}}]$ and $m^{\mathrm{AB}}(c,T) = m_0[cT_{\mathrm{m}}^{\mathrm{A}} + (1-c)T_{\mathrm{m}}^{\mathrm{B}} - T]$ with a constant m_0 related to the latent heat of the alloy. The thermodynamic model represented by this potential represents a lens-shaped phase diagram which describes perfectly miscible substances, known as ideal solutions, well. Minimization of the potential will automatically lead to the partitioning of the solute between the phases under the constraint of concentration conservation. From the principle of minimization of the free energy one derives.

$$\tau\dot{\phi} = -\left[\frac{\partial f}{\partial\phi} - \nabla\frac{\partial f}{\partial\nabla\phi}\right] = \epsilon\nabla^2\phi - \gamma^{\mathrm{AB}}\phi(1-\phi)\left(\frac{1}{2} - \phi + \frac{m^{\mathrm{AB}}(c,T)}{\gamma^{\mathrm{AB}}}\right), \tag{12}$$

$$\dot{c} = \nabla M_c c(1-c)\nabla\frac{\partial f}{\partial c} = \nabla\frac{M_c RT}{v_{\mathrm{m}}}\nabla c + \nabla M_c c(1-c)\nabla(f_{\mathrm{B}} - f_{\mathrm{A}}). \tag{13}$$

With $D = M_c RT/v_{\mathrm{m}}$ one recovers the diffusion equation in Fick's approximation but augmented by a term proportional to $\nabla(f_{\mathrm{B}} - f_{\mathrm{A}})$. This accounts for the partitioning of the solute in the interface. The model is however not restricted to this special form of the free energy functional. A generalized model can also be a mixture in ϕ of single-phase free energies (see, e.g. [28])

$$\tilde{f} = \tfrac{1}{2}\epsilon(\nabla\phi)^2 + \phi f_\alpha(c) + (1-\phi)f_\beta(c) \tag{14}$$

where the free energies $f_{\alpha/\beta}(c)$ in the bulk phases α or β, respectively, are convex functions in c. The important point of the model is that c is treated as continuous over the interface in the spirit of the Cahn–Hilliard model. This implies that the interfacial energy becomes intrinsically dependent on the local concentration and cannot be treated as an independent entity (see discussion in [29, 30]). A modification of the original WBM model by Warren *et al* [31] was used to simulate first dendritic structures in alloy solidification in 1995. This marks a breakthrough towards the application on real materials. Other important studies by the authors deal with solute trapping in rapid solidification [32, 33] and the effect of surface energy anisotropy in phase-field models [34, 35].

3. Theoretical background

In this section, some basic relations that help one to understand the underlying physics and which are indispensable for those who want to become active in developing phase-field models are reviewed. Thereafter the MDF model will be outlined.

3.1. Gibbs–Thomson limit

The notation in the previous section was adapted to the notation in the classical publications about phase-field models. Close to equilibrium, however, the model parameters can be related to physically measurable quantities like interfacial energy σ, interfacial mobility μ, deviation from thermodynamic equilibrium Δg and interfacial width η [36]. In the appendix these relations are derived from the traveling wave solution of the phase-field equation for three forms of the potential function: the so-called double well, the double obstacle and the top hat potential. The double obstacle will be used, as it has advantages in numerical calculations and is used in the latest version of the MPF method [37]. In the physical notation the free energy density and phase-field equation for $0 \leqslant \phi \leqslant 1$ become[3]

$$f = \left\{ \frac{\sigma}{\eta} \left[(\eta \nabla \phi)^2 + \pi^2 \phi (1-\phi) \right] + 2\pi h_{\mathrm{DO}}(\phi) \Delta g \right\} \frac{4}{\pi^2} \tag{15}$$

$$\dot{\phi} = \mu \left[\frac{\sigma}{\eta} \left(\eta \nabla^2 \phi + \frac{\pi^2}{\eta} \left(\phi - \frac{1}{2} \right) \right) - \frac{\pi}{\eta} \sqrt{\phi(1-\phi)} \Delta g \right] \tag{16}$$

with the 1D steady state solution of a traveling wave with velocity $v_n = \mu \Delta g$, see appendix equation (67)

$$\phi(x,t) = \frac{1}{2} - \frac{1}{2} \sin\left(\frac{\pi}{\eta} (x - v_n t) \right). \tag{17}$$

The notation of f in equation (15) is chosen to underline that in a phase-field model the interface is treated as a volume with excess energy density σ/η. The expression in the square brackets is a dimensionless measure of the structure of the interface. h_{DO} is a monotonous weighting function as defined in the appendix equation (64). The derivative of this function is proportional to the gradient of ϕ, $\nabla\phi = (\pi/\eta)\sqrt{\phi(1-\phi)}$. Now we face the paradox that in the phase-field equation (16) the first two terms proportional to $\eta\nabla^2\phi$ and $(\pi^2/\eta)(\phi - \frac{1}{2})$ diverge in the sharp interface limit $\eta \to 0$ as $\frac{1}{\eta}$[4]. To resolve this paradox we follow Caginalp [27] by expanding the Laplacian of a spherically symmetric problem in the radius coordinate ρ

$$\eta \nabla^2 \phi(x) = \eta \left(\frac{\partial^2 \phi}{\partial \rho^2} + \frac{1}{\rho} \frac{\partial \phi}{\partial \rho} \right) \tag{18}$$

$$= \frac{\pi^2}{\eta} \left(\frac{1}{2} - \phi \right) + \frac{\pi}{\rho} \sqrt{\phi(1-\phi)} + O\left(\frac{\eta}{\rho^2} \right). \tag{19}$$

Inserting this into (16) shows that the leading divergent terms $\sim 1/\eta$ exactly cancel out and the second term in (18) becomes the leading contribution proportional to the mean curvature $(1/\rho) = \kappa$. This is of course not a mere coincidence, but a consequence of the steady state solution. If the phase-field contour deviates from the steady state contour besides having a smooth curvature κ, the divergent terms will not cancel out and the resulting contributions will force the contour towards the steady state profile. This correction will be stronger the

[3] The double obstacle potential $\phi(1-\phi)$ is unbounded to $-\infty$ for $\phi < 0$ and $\phi > 1$. Therefore a cutoff or obstacle against unphysical values of ϕ at $\phi = 0$ and $\phi = 1$ has to be included—hence the name.

[4] Note that $\nabla^2\phi \sim 1/\eta^2$.

smaller η is. The phase field equation (16) or (1) therefore acts in two ways: firstly to stabilize the phase-field contour in the normal or radial direction through the interface, and secondly to evaluate the (mean) curvature of the interface. We find to lowest order of an expansion in $\eta\kappa_{\max} \ll 1$, where $\frac{1}{\kappa_{\max}}$ is the smallest length to be resolved, the equivalence to the Gibbs–Thomson equation

$$v_n = \dot{\phi}|\nabla\phi|^{-1} = \frac{\dot{\phi}\eta}{\pi\sqrt{\phi(1-\phi)}} = \mu(\sigma\kappa - \Delta g). \tag{20}$$

This limit is called the Gibbs–Thomson limit of the phase-field method where simulation results are independent of the interface width, which now can be scaled for numerical convenience. Spurious effects will, however, arise in the interface if the phase-field equation is coupled to a transport equation and the driving forces Δg are not constant. This will be shown in the section 3.3 after the effect anisotropy has been discussed briefly.

3.2. Anisotropy and the ξ-vector

Anisotropy of the interfacial energy and mobility reflects the atomistic crystallographic structure of interfaces in materials in a mesoscopic description. This anisotropy is weak for solid–liquid interfaces in most metallic materials (see section 4.1) or strong, leading to faceted interface structures as in silicon [38]. There is definitely an additional amplification by torque effects on the interface as described by Herring [39]. This torque is due to the fact that the minimum state of an interface is not only controlled by its curvature solely but by the variation of curvature and surface energy as a product. If the interfacial energy is a simple function of one angle θ the curvature undercooling in the Gibbs–Thomson equation becomes

$$\sigma\kappa \rightarrow (\sigma + \sigma'')\kappa, \tag{21}$$

where σ'' is the second derivative of σ with respect to θ. For the solid–liquid interface of a metal with cubic anisotropy the interfacial energy is mostly approximated $\sigma(\theta) = \sigma_0(1 + \delta\cos(4\theta))$ with a small anisotropy δ of the order of a few percent. It is easy to calculate that $\sigma'' = -16\sigma_0\delta\cos(4\theta)$, i.e. the torque becomes the dominating contribution in the Gibbs–Thomson equation, more than one magnitude higher than the interfacial energy anisotropy. Therefore, even metals with a small anisotropy will develop a noticeable anisotropy in the equilibrium and growth shape. Generally the interface energy will be a function of the interface normal with respect to the solid phase $\vec{n} = \nabla\phi/|\nabla\phi|$ in solidification. In solid–solid transformation, it is, in addition, a function of the misorientation of the adjacent solid phases. As the latter can be considered to be independent of the solution of the phase field we shall set it constant when only one interface between two phases is considered. The variation of the gradient energy term in the phase-field equation (6) in the physical notation (15) with respect to $\nabla\phi$ then becomes

$$\nabla\frac{\partial}{\partial\nabla\phi}\frac{\sigma(\vec{n})}{\eta}\left[(\eta\nabla\phi)^2 + \pi^2\phi(1-\phi)\right] = 2\eta\sigma(\vec{n})\nabla^2\phi + \nabla\xi(\vec{n})\frac{\left[(\eta\nabla\phi)^2 + \pi^2\phi(1-\phi)\right]}{\eta}, \tag{22}$$

where $\xi = \partial\sigma(\vec{n})/\partial\nabla\phi$ is the so-called ξ-vector representing the Herring torque generalized to the framework of the phase-field model [35]. The second term in equation (22) contributes strongly in anisotropic systems and triggers preferential growth of an interface in its weak direction. Although this contribution is essential for all physical systems, it will be omitted in the following derivation for readability. It does not interfere with the general model development strategy and can be added in straightforward manner.

3.3. The thin interface limit

As pointed out above, most applications of the phase-field method deal with the coupling of the motion of the interface to a long-range transport process, e.g. diffusion of the solute caused by solute redistribution at the interface during alloy solidification. As the velocity of the interface depends on the local supersaturation and thereby on the concentration profile within the interface, the driving force $\Delta g = \Delta g(c(\vec{x}))$ will not be constant if there is a significant concentration gradient on the scale of the interface width η used in the numerical calculation. One may divide the local supersaturation or, respectively, the local driving force Δg into two components: a constant part Δg^i which represents the kinetic driving force acting on the atomistic interface, and a varying part $\Delta\tilde{g}$ that stems from the diffusion gradient in the bulk material apart from the atomistic interface. The latter is, of course, physically correct, describing the bulk undercooling, but it should not contribute to the motion of the interface in the sense of the Gibbs–Thomson relation (20). If the interface width used in a numerical calculation exceeds the atomistic width, a scheme is needed to separate both of these contributions. This was developed by Karma and Rappel in 1996 [40, 41] for solidification of pure substances and later generalized by Karma and coworkers to alloy solidification [1, 42, 43]. Recently it was generalized to multicomponent alloys by Kim [44]. The following description ist based on Kim's deduction, but uses the double obstacle potential for consistency with the MPF model. The phase-field and liquid diffusion equation for a solid–liquid phase transition in a multicomponent alloy become (diffusion in solid is neglected)

$$\dot{\phi} = \mu^{\mathrm{eff}}\left[\sigma\left(\nabla^2\phi + \frac{\pi^2}{\eta^2}\left(\phi - \frac{1}{2}\right)\right) + \frac{\pi}{\eta}\sqrt{\phi(1-\phi)}\Delta g\right] \tag{23}$$

$$\dot{c}^i = \nabla M_{\mathrm{l}}^{ij}(1-\phi)\nabla\frac{\partial f^c}{\partial c_{\mathrm{l}}^j} + \nabla A^i\dot{\phi}\vec{n}. \tag{24}$$

μ^{eff} is an effective interface mobility as derived below. The chemical free energy $f^c = \phi f_{\mathrm{s}}(\{c_{\mathrm{s}}^i\}) + (1-\phi) f_{\mathrm{l}}(\{c_{\mathrm{l}}^i\})$ is treated as a function of the phase concentrations c_{s}^i and c_{l}^i in solid and liquid which sum up to the mixture concentration $c^i = \phi c_{\mathrm{s}}^i + (1-\phi)c_{\mathrm{l}}^i$ [29]. The sum convention over double composition indices i is used for readability. The concentrations are vectors in the space of the components i of a multicomponent alloy. $\{M_{\mathrm{l}}^{ij}\}$ is the mobility matrix in liquid. The last term in equation (24) is the gradient of the so-called anti-trapping current $j_{\mathrm{A}}^i = A^i\dot{\phi}\vec{n}$ introduced by Karma [1] to compensate for asymmetrical fluxes in the interfacial region if the diffusivity within the two phases differs significantly. It is directed in normal direction $\vec{n} = \nabla\phi/|\nabla\phi|$ and proportional to the local phase change $\dot{\phi}$. The anti-trapping function $A^i = A^i(c^i, \phi)$ will be determined by the condition of a vanishing potential jump as explained in figure 3. The derivation is only sketched here and the reader is referred to the original literature [1, 42, 43, 44]. In steady state motion of a planar solidification front (1D) with velocity v_n in positive direction equation (24) can be expressed as

$$-v_n\frac{\mathrm{d}c}{\mathrm{d}x} = \frac{\mathrm{d}}{\mathrm{d}x}D_{\mathrm{e}}^{ij}(1-\phi)\frac{\mathrm{d}c_{\mathrm{l}}^j}{\mathrm{d}x} - \frac{\mathrm{d}}{\mathrm{d}x}A^i v_n\frac{\mathrm{d}\phi}{\mathrm{d}x}. \tag{25}$$

Integration over the whole system yields

$$v_n(c_{\mathrm{s}}^i - c^i) = D_{\mathrm{l}}^{ij}(1-\phi)\frac{\mathrm{d}c_{\mathrm{l}}^j}{\mathrm{d}x} - v_n A^i\frac{\mathrm{d}\phi}{\mathrm{d}x}, \tag{26}$$

$$v_n(1-\phi)(c_{\mathrm{s}}^i - c_{\mathrm{l}}^i) \approx D_{\mathrm{l}}^{ij}(1-\phi)\frac{\mathrm{d}c_{\mathrm{l}}^j}{\mathrm{d}x} + v_n A^i\frac{\pi}{\eta}\sqrt{\phi(1-\phi)}. \tag{27}$$

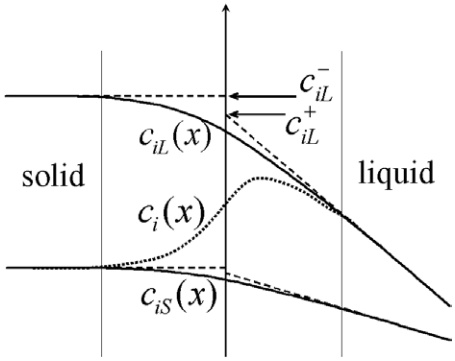

Figure 3. Sketch of the solute profile in the interface. The straight lines indicate extrapolations from the edge of the interface into the center. Without correct anti-trapping there will be a jump in the extrapolated concentrations which corresponds to a potential jump at the interface and has to be avoided. Reproduced with permission from [44], © Elsevier 2007.

The solid concentration c_s^i is constant for vanishing solid diffusion. $D_l^{ij} = M_l^{ik}(\partial^2 f^c/\partial c_l^j \partial_l^k)$ is the diffusion matrix in liquid and the gradient of the phase-field contour was approximated by the steady state solution (17) or (67). Inverting this we have the concentration gradient

$$\frac{\mathrm{d}c_l^i}{\mathrm{d}x} = v_n[D_l^{ij}]^{-1}\left[(c_s^j - c_l^j) - A^i \frac{\pi}{\eta}\frac{\sqrt{\phi(1-\phi)}}{(1-\phi)}\right]. \tag{28}$$

It can then be shown (see equation (37) in [44]) that a steady state solution of the concentration profile is found if the concentration gradient in liquid is proportional to the phase field of liquid $(1-\phi)$

$$\frac{\mathrm{d}c_l^i}{\mathrm{d}x} = (1-\phi)\frac{\mathrm{d}c_l^i}{\mathrm{d}x}|_{\phi=0} = v_n(1-\phi)[D_l^{ij}]^{-1}(c_s^i - c_l^i). \tag{29}$$

This means nothing else than that the local fluxes per density of the liquid phase are constant and proportional to the velocity of the front times the concentration jump between the phases. This condition can now be used to solve (28) and (29) for A^i and we then arrive at the final diffusion equation with anti-trapping current

$$\dot{c}^i = \nabla M_l^{ij}(1-\phi)\nabla\frac{\partial f^c}{\partial c_l^j} + \nabla\frac{\eta}{\pi}\sqrt{\phi(1-\phi)}(c_s^i - c_l^i)\dot{\phi}\vec{n}. \tag{30}$$

The anti-trapping current in the diffusion equation compensates the asymmetry in fluxes on both sides of the interface in the limit of vanishing diffusivity in one phase. Historically this was the second step in the development of the thin interface limit. The first step had the decomposition of the driving force in interface undercooling and bulk undercooling in the phase-field equation. Like the diffusion equation we transform the phase-field equation in the moving frame system in steady state and 1D approximation

$$-v_n\frac{\mathrm{d}\phi}{\mathrm{d}x} = \mu^{\mathrm{eff}}\frac{\pi}{\eta}\sqrt{\phi(1-\phi)}\Delta g \approx -\mu^{\mathrm{eff}}\frac{\mathrm{d}\phi}{\mathrm{d}x}\Delta g. \tag{31}$$

Integration over x yields

$$v_n\int_{-\infty}^{\infty}\frac{\mathrm{d}\phi}{\mathrm{d}x}\mathrm{d}x = \mu^{\mathrm{eff}}\int_{-\infty}^{\infty}\Delta g\frac{\mathrm{d}\phi}{\mathrm{d}x}\mathrm{d}x = \mu^{\mathrm{eff}}\left[\Delta g^i - \int_{-\infty}^{\infty}\phi\frac{\mathrm{d}\Delta g}{\mathrm{d}x}\mathrm{d}x\right]. \tag{32}$$

The partial integration has split the driving force into the constant contribution Δg^i, which is considered to be the physical contribution acting on the interface and the varying contribution proportional to the gradient of Δg. In the dilute solution limit we may approximate $\Delta g = \Delta S(T_\mathrm{m} + m_\mathrm{l}^i c_\mathrm{l}^i - T)$, with the liquidus slope $m_\mathrm{l}^i < 0$. For constant temperature and using (29) for the concentration gradient we can evaluate the integrals

$$\frac{\mathrm{d}\Delta g}{\mathrm{d}x} = \Delta S m_\mathrm{l}^i \frac{\mathrm{d}c_\mathrm{l}^i}{\mathrm{d}x} = \Delta S m_\mathrm{l}^i v_n (1-\phi)[D_\mathrm{l}^{ij}]^{-1}(c_\mathrm{s}^j - c_\mathrm{l}^j), \tag{33}$$

$$v_n = \mu^\mathrm{eff}\left\{\Delta g^i - v_n \frac{\eta}{8}\Delta S m_\mathrm{l}^i [D_\mathrm{l}^{ij}]^{-1}(c_\mathrm{s}^j - c_\mathrm{l}^j)\right\}. \tag{34}$$

The spurious driving force due to the concentration gradient in the interface is within the given approximation proportional to the interface velocity v_n. Consequently, one can handle it as a systematic perturbation and define an equivalent to the Gibbs–Thomson equation (20) with an effective mobility μ_eff

$$v_n = \frac{\mu^\mathrm{eff}}{1 - \mu^\mathrm{eff}\frac{\eta}{8}\Delta S m_\mathrm{l}^i [D_\mathrm{l}^{ij}]^{-1}(c_\mathrm{s}^j - c_\mathrm{l}^j)}\Delta g^i = \mu \Delta g^i. \tag{35}$$

The last equation is simply the definition of the physical mobility μ as the proportionality constant between velocity and (physical) driving force. It can be inverted to define the effective mobility $\mu^\mathrm{eff} = \mu/(1 + \mu\frac{\eta}{8}\Delta S m_\mathrm{l}^i [D_\mathrm{l}^{ij}]^{-1}(c_\mathrm{s}^j - c_\mathrm{l}^j))$[5]. Having the effective mobility one can reproduce the physically correct relation (35) by solving relation (31) which evaluates the spurious local driving force Δg. Whereas in the sharp interface limit $\eta \to 0$ the correction vanishes and $\mu^\mathrm{eff} \to \mu$, it dominates for finite η and large physical mobilities μ. For $\mu \to \infty$ the effective mobility becomes independent of μ and the effect of anisotropic attachment kinetics that would be reflected by an anisotropy of μ is lost in the equation. This case corresponds to a phase transformation under diffusion control, where attachment is considered to not be rate determining and the neglect of its anisotropy should be tolerable. There may, however, be cases of strong anisotropy that can only be handled with a very high resolution of the interface.

3.4. The MPF model

The previous descriptions considered dual phase change problems, basically a solid–liquid phase change. The austenite to ferrite transformation in steel and other solid phase changes can also be treated in this framework [45]. Early phase-field models for a three-phase change problem, were developed by Karma [46] and Wheeler *et al* [47] for eutectic systems. They consist of a dual phase-field model (for solid and liquid) superposed by a Cahn–Hilliard model for demixing in the solid. Thus they are restricted to a three-phase transformation. To be applicable to an arbitrary number of different phases or grains of the same phase, but distinct by their orientation, the so-called MPF model was developed [29, 37, 48–50]. Each grain α distinct from others either by its orientation or phase (or both) is attributed by its individual phase field ϕ_α. Historically this can be seen as a vector-order-parameter model in Landau's sense [9]. A similar model to the MPF was developed contemporaneously by Fan and Chen [51, 52]. Later Kobayashi and Warren [53] developed a model that uses the grain

[5] As is always the case, the signs are important. With negative M_l and $c_\mathrm{s} - c_\mathrm{l}$ the denominator of μ^eff is always finite and positive. The denominator in (35) will however approach 0 if $\mu^\mathrm{eff}(\eta/8)\Delta S m_\mathrm{l}^i [D_\mathrm{l}^{ij}]^{-1}(c_\mathrm{s}^j - c_\mathrm{l}^j) \to 1$, which corresponds to the situation of infinite physical mobility. However, in a numerical simulation one has to be careful that μ_eff does not exceed this value. Otherwise the sign of the physical mobility becomes negative which will automatically lead to oscillations in the calculation.

orientation as an order parameter and allows simulating of solidification, grain growth and grain rotation in a multi-grain structure. The reader is referred to the respective literature.

We start from a general free energy description separating different physical phenomena, interfacial f^{intf}, chemical f^{chem} and elastic energy f^{elast}

$$F = \int_{\Omega} f^{\text{intf}} + f^{\text{chem}} + f^{\text{elast}} \tag{36}$$

other contributions like magnetic and electric energy may be added in future applications.

$$f^{\text{intf}} = \sum_{\alpha,\beta=1,..,N,\alpha\neq\beta} \frac{4\sigma_{\alpha\beta}}{\eta_{\alpha\beta}} \left\{ -\frac{\eta_{\alpha\beta}^2}{\pi^2} \nabla\phi_\alpha \cdot \nabla\phi_\beta + \phi_\alpha\phi_\beta \right\}, \tag{37}$$

$$f^{\text{chem}} = \sum_{\alpha=1,..,N} h(\phi_\alpha) f_\alpha(c_\alpha^i) + \tilde{\mu}^i (c^i - \sum_{\alpha=1,..,N} \phi_\alpha c_\alpha^i) \tag{38}$$

$$f^{\text{elast}} = \frac{1}{2} \left\{ \sum_{\alpha=1,..,N} h(\phi_\alpha)(\bar{\epsilon}_\alpha - \bar{\epsilon}_\alpha^* - c_\alpha^i \bar{\epsilon}_\alpha^i) \bar{\bar{C}}_\alpha (\bar{\epsilon}_\alpha - \bar{\epsilon}_\alpha^* - c_\alpha^j \bar{\epsilon}_\alpha^j) \right\}. \tag{39}$$

Again I use the sum convention over double indices of the components i. $N = N(x)$ is the local number of phases and we have the sum constraint[6]

$$\sum_{\alpha=1,..,N} \phi_\alpha = 1. \tag{40}$$

$\sigma_{\alpha\beta}$ is the energy of the interface between phase—or grain—α and β. It may be anisotropic with respect to the relative orientation between the phases. $\eta_{\alpha\beta}$ is the interface width and will be treated equal for all interfaces in the following. The chemical free energy is built from the bulk free energies of the individual phases $f_\alpha(\vec{c}_\alpha)$ which depend on the phase concentrations c_α^i. $\tilde{\mu}^i$ is the generalized chemical potential or diffusion potential of component i introduced as a Lagrange multiplier to conserve the mass balance between the phases $c^i = \sum_{\alpha=1,..,N} \phi_\alpha c_\alpha^i$. The elastic part of the free energy is defined based on the elastic properties and strain related to the different phases: the total strain tensor $\bar{\epsilon}_\alpha$ in phase α, the eigenstrain of transformation $\bar{\epsilon}_\alpha^*$, the chemical expansion of component i $\bar{\epsilon}_\alpha^i$ in Vegard approximation and the elasticity matrix $\bar{\bar{C}}_\alpha$.

For $N = 2$ the interfacial energy reduces to the one for the dual phase field (15) with $\phi_2 = 1 - \phi_1$ and $\nabla\phi_2 = -\nabla\phi_1$. Although the double well potential was used in the interfacial energy in the original version of the MPF [48], due to several advantages the double obstacle potential seems preferential today. It has two main advantages. Firstly, the phase-field variables converge to 0 and 1 within the prescribed interface width η, which makes it easier to store the interface information and to reduce memory in a numerical calculation. The software MICRESS [54] based on the model, stores only relevant information in regions characterized as bulk phases, interface, triple or multiple junctions. Secondly, the double obstacle potential suppresses the spreading out of multiple junctions into the interface region, as known from the double well potential. The latter is cubic in the phase-field variable, which energetically favors multiple junctions. This can be easily demonstrated by considering the center of a dual interface in contact with a triple junction, or equivalently the nucleation of a third phase ϕ_3 in the center of an interface. With $\phi_1 = \phi_2 = \frac{1}{2}(1 - \phi_3)$ the potential energy f_n, where $n = 1$

[6] This constraint is not included in Fan and Chen's model [52].

stands for the double obstacle and $n = 2$ for the double well, becomes

$$\begin{aligned} f_n &= \phi_1^n\phi_2^n + \phi_1^n\phi_3^n + \phi_2^n\phi_3^n \\ &= \frac{1}{4}(1-\phi_3)^{2n} + (1-\phi_3)^n\phi_3^n \qquad (41) \\ &= \frac{1}{4} + \frac{\phi_3}{2} + O(\phi_3^2) \qquad \text{for } n = 1 \\ &= \frac{1}{4} - \phi_3 + O(\phi_3^2) \qquad \text{for } n = 2. \qquad (42) \end{aligned}$$

In the limit $\phi_3 \to 0$ $\mathrm{d}f_1/\mathrm{d}\phi_3$ is positive for the double obstacle, i.e. there is a natural barrier against growth of a third phase. For the double well $\mathrm{d}f_2/\mathrm{d}\phi_3$ is negative, i.e. the growth of the third phase reduces the potential energy and the dual interface becomes intrinsically unstable. Then a strong counter-energy is needed to suppress spreading out of the multiple junctions. An alternative approach to avoid the given problem is described in [55, 56], where a special type of a potential function that guarantees the stability of dual interfaces is constructed. This formulation, however, is restricted to triple junctions and will be difficult to generalize.

The MPF equations are derived (for details see [49])

$$\dot{\phi}_\alpha = -\sum_{\beta=1,..,N} \frac{\pi^2}{8\eta N}\mu_{\alpha\beta}\left(\frac{\delta F}{\delta\phi_\alpha} - \frac{\delta F}{\delta\phi_\beta}\right). \qquad (43)$$

This is a superposition of dual phase changes between pairs of phases. $\mu_{\alpha\beta}$ is defined individually for each pair of phases and can be treated in the thin interface limit replacing it by the effective mobility (35). Inserting the free energy (36) to (39) we calculate explicitly

$$\dot{\phi}_\alpha = \sum_{\beta=1,..,N} \frac{\mu_{\alpha\beta}}{N}\left\{\sum_{\gamma=1,..,N}[\sigma_{\beta\gamma} - \sigma_{\alpha\gamma}]I_\gamma + \frac{\pi^2}{8\eta}h'\Delta g_{\alpha\beta}\right\}, \qquad (44)$$

$$I_\gamma = \nabla^2\phi_\gamma + \frac{\pi^2}{\eta^2}\phi_\gamma. \qquad (45)$$

I_γ is the generalized curvature term. For anisotropic interfacial energies the respective torque term has to be added (see section 3.2). $\Delta g_{\alpha\beta}$ comprises the derivative of the chemical free energy and the elastic free energy with respect to the phase-field variables. There arises, however, a consistency problem that remains unsolved to date: how to formulate an appropriate contour function $h(\phi_\alpha)$ for multiple junctions. A thermodynamically consistent form is the unity $h(\phi_\alpha) = \phi_\alpha$ with $h' = 1$. However, this disturbs the traveling wave solution of the double obstacle potential, as described in detail in the appendix. A generalization of the contour function h_{DO} (64) which is suitable for multiple junctions and does not violate the sum constraint $\sum_{\alpha=1,..,N} h(\phi_\alpha) = 1$ hardly seems possible. In most simulations using the MPF the so-called antisymmetric approximation, which resigns from thermodynamic consistency at the multiple junctions, is thus used.

$$\dot{\phi}_\alpha = \sum_{\beta=1,..,N} \mu_{\alpha\beta}\left\{\sigma_{\alpha\beta}\left[\phi_\beta\nabla^2\phi_\alpha - \phi_\alpha\nabla^2\phi_\beta + \frac{\pi^2}{2\eta^2}(\phi_\alpha - \phi_\beta)\right] + \frac{\pi}{\eta}\sqrt{\phi_\alpha\phi_\beta}\Delta g_{\alpha\beta}\right\}. \qquad (46)$$

The chemical free energy (38) in the MPF is evaluated from the phase concentration c_α^i in the individual phases α. In the interface region, the concentration has to be split into the phase concentrations and an extra condition is needed to fix the additional degrees of freedom. In the original model [29], a symmetric deviation from equilibrium in each pair of phases was used. Kim *et al* [30] proposed the condition of equal diffusion potential $\delta f/\delta c_\alpha^i$ of pairs of

phases in the interface, called a quasi-equilibrium condition. It only implies the equality of the chemical potential up to a constant factor which defines the chemical driving force on the interface. This condition is also used in the thermodynamically consistent derivation of the actual MPF model [37]. The splitting of the concentrations into phase concentrations and the evaluation of the quasi-equilibrium condition is computationally demanding. However, it must be considered indispensable for quantitative simulations in the thin interface limit. An extrapolation scheme of the local quasi-equilibrium condition for computational efficiency is presented in [37].

For a multicomponent system, a set of k diffusion equations for all solute components, which are generally not independent but linked by cross terms, is required. These equations are derived for the conserved compositions c^i from the free energy functional by a relaxation approach.

$$\begin{aligned}\dot{c^i} + \vec{u}\cdot\nabla c^i_{\text{liquid}} &= \nabla\left\{\sum_{\alpha=1}^{N}\phi_\alpha M^{ij}_\alpha(\{c^j_\alpha\})\nabla\frac{\delta F}{\delta c^j_\alpha} + \sum_{\alpha,\beta=1}^{N} j^i_{\alpha\beta}\right\}\\ &= \nabla\left\{\sum_{\alpha=1}^{N}\phi_\alpha[D^{ij}_\alpha\nabla c^j_\alpha - \nabla M^{ij}_\alpha\bar{\epsilon}^j_\alpha\bar{s}_\alpha] + \sum_{\alpha,\beta=1}^{N} j^i_{\alpha\beta}\right\},\end{aligned} \tag{47}$$

$$j^i_{\alpha\beta} = b\eta\sqrt{\phi_\alpha\phi_\beta}\left((c^j_\alpha(x) - c^j_\beta(x))\frac{D^{ij}_\alpha - D^{ij}_\beta}{D^{ij}_\alpha + D^{ij}_\beta}\right)\dot{\phi}\cdot\frac{\phi_\beta\nabla\phi_\alpha - \phi_\alpha\nabla\phi_\beta}{|\phi_\beta\nabla\phi_\alpha - \phi_\alpha\nabla\phi_\beta|}. \tag{48}$$

The diffusion equation is a straightforward extension of the single component dual phase diffusion equation (30) with the diffusion matrices in the individual phases $D^{ij}_\alpha = M^{ik}(\partial^2 F/\partial c^k\partial c^j)$ considering multiple components, cross effects between the components and diffusion in all phases. Advective transport in the liquid phase ϕ_{liquid} is considered with velocity $\vec{u}$. The anti-trapping flux $j^i_{\alpha\beta}$ is an extrapolation to diffusion in all phases as a superposition of the fluxes in the different interfaces. It reduces in the limit of vanishing diffusion in one phase or equal diffusion in both phases to the standard expression. It is easy to check that for non-vanishing diffusion in all phases the given anti-trapping current is a superposition of a symmetric model (equal diffusion in both phases, where no anti-trapping current is needed) and the one-sided model which neglects diffusion in one of the phases. Weighting the diffusivities in the given way results in the correct diffusion in the phase mixture. The second term in the diffusion equation proportional to the gradient of the hydrostatic stress $\bar{s}_\alpha = \bar{\bar{C}}_\alpha(\bar{\epsilon}_\alpha - \bar{\epsilon}^*_\alpha - \bar{\epsilon}^i_\alpha c^i)$ is also of note. This stress drives and additional diffusion flux if the Vegard coefficient $\bar{\epsilon}^i_\alpha$ of the respective phase and component is nonzero.

The mechanical equilibrium equation follows in quasi-static approximation

$$0 = \nabla\frac{\delta F}{\delta\epsilon} = \nabla\sum_{\alpha=1}^{N}\phi_\alpha\bar{\bar{C}}_\alpha(\bar{\epsilon}_\alpha - \bar{\epsilon}^*_\alpha - c^i_\alpha\bar{\epsilon}^i_\alpha). \tag{49}$$

Phase field and concentration enter the mechanical equilibrium equation naturally. Reversely, the stress distribution couples to both the phase-field and diffusion equation. Thus all three equations are closely coupled. It will be demonstrated later in section 4.6 how the consistent consideration of this coupling can be crucial for the explanation of growth kinetics of pearlite [57].

Finally, the coupling of the phase field to flow in the liquid phase will be explained. As there is only a negligible influence of flow and pressure on the phase stability in metallic systems, this coupling acts only indirectly by the modification of the transport in liquid. Nevertheless,

this can be quite significant as shown in section 4.3. The equations for fluid flow and mass conservation read [58]

$$\frac{\partial}{\partial t}[\vec{u}(\phi_{\text{liquid}})] + \nabla[\phi_{\text{liquid}}\vec{u}\vec{u}]$$
$$= \nabla[\nu\nabla\vec{u}\phi_{\text{liquid}}] - \frac{\phi_{\text{liquid}}}{\rho_0}\left[\nabla p + \frac{\partial\rho}{\partial c}(c_1 - \langle c_1\rangle)\vec{g}\right] - h^*\frac{\nu\phi^2\phi_{\text{liquid}}\vec{u}}{\eta^2} \tag{50}$$

$$\nabla\cdot\left[\phi_{\text{liquid}}\vec{u}\right] = 0. \tag{51}$$

ν is the liquid viscosity, ρ_0 the average melt density, p the melt pressure, $\partial\rho/\partial c^i$ the linear coefficient of density change with the i component, $\langle c_1^i\rangle_g$ the global average melt concentration, $\vec{g}$ the gravity vector. The last term in equation (50) represents the friction of the melt on the resting solid. It is shown in [58] that the no-slip condition in the diffuse interface is fulfilled with an uniquely defined integration constant h^* independent of the actual value of the interface thickness. Examples are given in [59–62]. An alternative approach to the coupling of fluid flow and phase-field calculations was developed by Anderson *et al* [63, 64]. They employ a continuous viscosity change between solid and liquid to distinguish the transport properties of the phases. This approach has the advantage that the moving solid can be incorporated easily by treating it as a highly viscous fluid. However, it suffers from convergence problems if the solid is treated as rigid and it violates the no-slip condition in the thin interface limit. Further theoretical investigations are presented by Kassner and coworkers [65].

4. Examples

4.1. Equiaxed dendritic solidification

Solidification of metallic alloys is an important application for phase-field simulation. The underlying physics have been well described by the Gibbs–Thomson relation for the interface velocity coupled to redistribution of heat and solute at the interface and long-range transport in the bulk phases, commonly referred to as the Stefan problem. Interfacial anisotropy is weak and, in good approximation, can be treated as a perturbation of a spherical Wulff shape. Negligible stresses develop on the interface during growth even if solid and liquid differ in density. Heat conduction in both phases is nearly identical and solute diffusion in solid can be neglected in comparison with solute diffusion in the melt. The only influence that troubles researchers is convection in the melt. This is difficult to treat analytically or numerically, but unavoidable under terrestrial conditions (see below). Experimentation under reduced gravity is needed to establish benchmark data for validation of theories and simulations under diffusion controlled conditions [66]. Where does the theoretical interest in dendritic solidification come from if everything is so easy? Firstly, a solidification front growing into an undercooled melt is intrinsically unstable [67] and a dendrite can be viewed as a self-organizing structure. Secondly, the analytical solution of steadily growing dendrite approximated by a parabola of revolution is a self-similar solution that does not select the absolute scale, i.e. it fails to predict the scale of the solidification microstructure whereas nature correlates the scale of the microstructure to the material and process conditions well. This problem was only solved quite recently by the microscopic solvability theory [13, 69]. The mechanism is the amplification of microscopic fluxes (thermal or solutal) at the dendrite tip, caused by surface tension anisotropy. The amplification is due to the long-range diffusion fields around the tip, which are interlinked with the tip shape. To date, the phase-field method is the most appropriate numerical method that can bridge the different length scales from the capillarity length of a few nanometers, where the interfacial anisotropy acts, to the millimeter scale of diffusions. Figure 4 shows

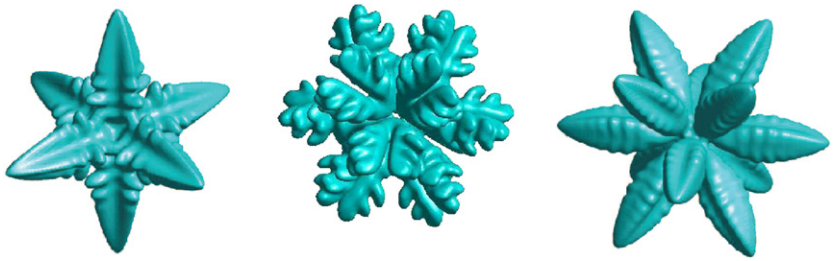

Figure 4. Phase-field simulations of dendritic growth with different modes of surface tension anisotropy. Left: cubic anisotropy with branches in the [1 0 0] directions. Middle: intermediate state between the [1 0 0] and [1 1 0] directions. Right: anisotropy with branches in the [1 1 0] directions. Reproduced by permission of the *MRS Bulletin* [68].

(This figure is in colour only in the electronic version)

three different equiaxed dendritic growth structures where the interfacial energy as a function of the orientation of the interface normal $\vec{n}$, $\sigma(\vec{n})$ has been varied (reproduced from [70]). The interfacial energy is expanded in spherical harmonics with cubic symmetry K_i with the Euler angles θ, Ψ ([71]).

$$\sigma(\theta, \Psi) = \sigma_0[1 + \epsilon_1 K_1(\theta, \Psi) + \epsilon_2 K_2(\theta, \Psi)] \tag{52}$$

the anisotropy coefficients ϵ_i are in the percent range for metallic systems and the anisotropy is hardly visible in the Wulff plot. The first cubic harmonic is known to favor the commonly observed [1 0 0] directions (figure 4, left). However, there is strong evidence [72] that the second term in (52) plays a significant role in some metals. In particular in Al–Zn alloys a transition from [1 0 0] dendrites to [1 1 0] dendrites is observed with varying [73]. This can be reproduced by reducing the prefactor of the first harmonic and keeping the second harmonic with a fixed negative value. The intermediate state shows quite a complicated structure that originates from the competition of different crystallographically preferred growth structures (figure 4, middle). The right dendrite shows clear preferential directions in the [1 1 0] directions. It must be emphasized yet again that the dendritic growth structure is a result of self-organization of the unstable solidification front with a very weak trigger given by the interfacial energy anisotropy. Phase-field simulations capture the underlying physics and make it tractable on a computer.

4.2. Spacing selection in directional growth

In directional dendritic solidification, an array of primary dendritic trunks growing along the temperature gradient forms a band of stable spacings, the mean value of which decreases with increasing growth velocity and increasing temperature gradient. This is described well by the classical models of Hunt and Kurz [74, 75]. It can be compiled in the simple form (see [76])

$$\bar{\lambda} = f_{\mathrm{D}} \sqrt{l_{\mathrm{s}} r_{\mathrm{tip}}}, \tag{53}$$

where $\bar{\lambda}$ is the mean spacing, $l_{\mathrm{s}} = M_{\mathrm{l}}(1-k)c_0/kG_z$ is the length of the mushy zone or solidification length with the liquids slope M_{l}, the partition coefficient k and the initial liquid concentration c_0 of a binary melt and the temperature gradient in the z-direction G_z. r_{tip} is the dendrite tip radius and f_{D} a geometrical factor. In a recent phase-field study of this problem, I was able to demonstrate that a sharp minimum of the band of stable states exists, which depends on the interfacial anisotropy in a similar way as the selection of the tip radius [77]. A sharp upper limit of the stable band does not exist, but if there is an effective splitting mechanism by side-branching the upper limit, from geometrical reasons, it is simply twice the

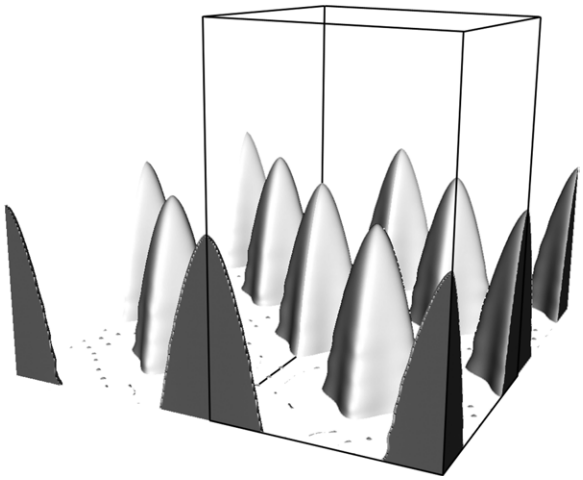

Figure 5. Snapshot of a stable array in directional dendritic solidification of AlCu. No noise is added therefore side-branching is low in the calculation. The actual calculation box is indicated. Reproduced with permission from [77], © Elsevier 2008.

lower limit [78]. Figure 5 shows a stable configuration of a dendritic array. The limit of the spacing can be investigated by narrowing the box size of the calculations. The observation that the tip radius and shape depends weakly on the spacing, i.e. a narrow spacing hinders growth down in the interdendritic region and narrows the tip shape, was used to reveal the mechanism determining this limit. This mechanism competes with the deviation of the tip shape from a parabola of revolution due to interface anisotropy. In [77] the radii evaluated by parabolic fits in the direction of fastest and slowest growth, were used to characterize the tip (r_{tip}) and the trunk (r_{trunk}). Typically for stable growth $r_{\text{tip}} < r_{\text{trunk}}$. Figure 6 shows the evaluated radii as a function of the spacing. Surprisingly there is a crossover of the radii[7]. For the critical spacing, the effect of interacting solutal fields of neighboring dendrites (in the periodic array) cancels the effect of interface anisotropy and an almost perfect parabolic fit is reached. Vanishing effective interface anisotropy should, according to the notion of the microscopic solvability theory lead to a destabilization of tip growth. In fact, the corresponding spacing lies exactly within the range, where destabilization of stable array growth is observed in simulations starting with several independent dendritic tips (see insert in figure 6). This observation demonstrates that the interfacial anisotropy, which acts on the atomistic scale of the capillarity length, is amplified even far beyond the scale of the dendrite tip to the scale of the dendritic spacing. It is amplified even further if we include another mechanism of transport: convection.

4.3. Spacing selection in binary alloy with buoyancy-driven convection

The problem discussed in this section is the influence of buoyancy-driven interdendritic flow on the selection of primary spacing in directional growth and the mutual interplay of convection with growth. On the one hand, convective transport of solute significantly alters the growth conditions. On the other hand, the magnitude of convection depends critically on solute gradients due to growth and on friction of the convecting liquid melt between the dendritic trunks. Because of this delicate interplay and because the long-range convective transport widens the amplification of interfacial instabilities again, a high theoretical interest

[7] For the evaluation of the spacing, only one dendrite was simulated in a fixed box and therefore situations below the stable band can also be examined.

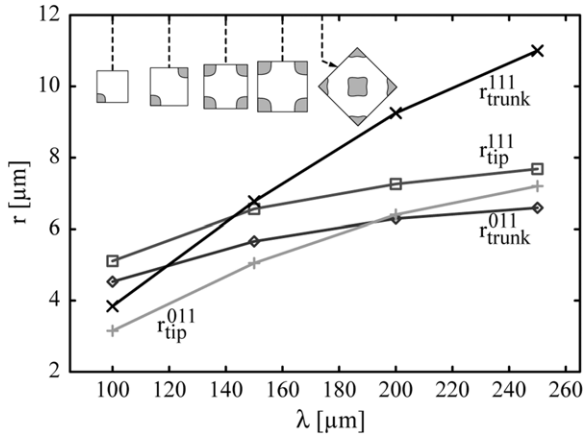

Figure 6. Plot of $r^{[1\,1\,1]}_{\mathrm{tip/trunk}}$ and $r^{[0\,1\,1]}_{\mathrm{tip/trunk}}$ for different spacings. The inserts show the stable configuration of tip growth in the boxes with the respective spacing. Reproduced with permission from [77], © Elsevier 2008.

in this problem arises. A high practical interest arises because convection in dendritic alloy solidification is inevitable due to density differences in the liquid melt. The density of metallic material depends strongly on the solute content, and due to solute redistribution at the growing solidification front, the concentration gradient around the dendritic tips is steep. Although the magnitude of this effect varies according to the alloy and the growth conditions, there will always be radial gradients with respect to the direction of gravity, and there is no stable regime against the onset of flow. Moreover, in most alloys and under technically feasible temperature gradients, the solutal density change is two orders of magnitude higher than the thermal density change. A stabilization of flow due to a stable temperature configuration is thus not effective. Here I am going to give an example of directional solidification of an Al–Cu alloy with a Cu concentration $c_0 = 4\,\mathrm{at\%}$ (from [82]).

Figure 7 shows a snapshot of typical simulation results calculated in a moving frame [79]. In figure 7(*a*) the gravity vector is pointing in a positive z-direction with a magnitude of $g = 3g_\mathrm{t}$ in units $g_\mathrm{t} = 9.81\,\mathrm{m\,s^{-2}}$ of the terrestrial gravity constant. Due to segregation of the heavy copper into the interdendritic melt, the density increases close to the dendrite and the melt is upwardly buoyant. In the following section, this will be termed upward flow. Unstable plumes form and the copper–enriched melt is washed out into the bulk liquid region. In figure 7(*a*), we can observe the transient from initial seeding of two solids at the bottom of the calculation domain into a fully developed dendritic array with mean spacing around $200\,\mu\mathrm{m}$. Obviously neither the solid structure nor the convective pattern reaches a steady state. This is because the temporarily leading dendrites trigger the melt flow by stopping transversal flow and supporting new upward flow in a low friction area. On the other hand, the upward flow transports segregated copper along the dendrite into the tip region, which slows down growth. The dendrites that have fallen back now face downward flow, created by more advanced neighboring dendrites. This downward flow transports melt relatively low in copper and enhances growth. In this manner, convection and growth of neighboring tips are connected by an oscillating interaction. This picture explains experimental findings, made by Mathiesen and Arnberg [80], of oscillating tip growth revealed by *in situ* synchrotron radiation imaging of the dendritic solidification structures in a thin sample.

Reverting the vector of gravity in downward direction leads to a completely different picture (see figures 7(*b*) and (*c*)). Downwardly buoyanced melt leads to an enrichment of

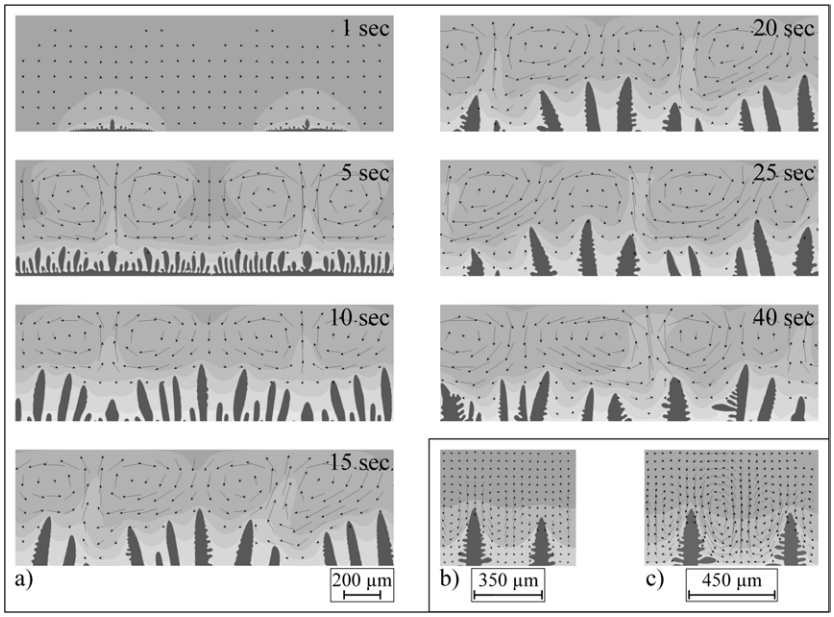

Figure 7. Concentration and flow profile in directional dendritic growth. The solid dendrites are of lower Cu concentration and appear dark grey. (*a*) upward buoyancy +3g. The time sequence starts after seeding of two crystals at the bottom of the domain. The solid spreads and forms side branches that evolve to a dendritic array. Between 5 s and 10 s the moving frame sets in to keep the leading tip at fixed position, withdrawing the whole domain one grid spacing to the bottom and adding a new layer with initial concentration c_0 at the top. The dendrite spacing adjusts to approximately 200 μm. Maximum flow speed 800 μ m s^{-1}. (*b*) downward buoyancy -1g. 350 μm spacing is metastable. Maximum flow speed 33 μm s^{-1} (*c*) downward buoyancy -1g. 450 μm spacing is stable. Maximum flow speed 50 μm s^{-1}. Reproduced with permission from [82], © Elsevier 2009.

copper in the interdendritic region. In contrast to upward buoyancy, the mean spacing is significantly increased (>400 μm for -1 g). This is clearly due to the enrichment of copper at the base of the dendrites. The convecting rolls are now confined to the interdendritic region and a stable flow pattern is established. To characterize the dependence of the spacing on the magnitude of flow more precisely, a number of simulations with fixed domain size and two initial seeds set in regular spacing seeking for the minimum stable spacing was performed. Stable growth in downward flow is characterized by symmetrical convection rolls and the two tips at equal position in the moving frame of the calculation.

Figure 8 provides a stability map of all calculations performed, classified in unstable, metastable and stable states. Taking the minimum stable spacing for all gravity levels under consideration, and noting that the average spacing is a multiple close to 1.5 of the minimum spacing, we can plot the average spacing, normalized by the average spacing at 0g versus the gravity level. Figure 9 shows the calculated spacings together with experimental results from solidification experiments in a centrifuge by Battaile *et al* [81] and a scaling relation recently derived [82].

4.4. Orientation selection in dendritic growth of Mg–Al

Mg-based alloys are gaining increasing technical importance due to the high demand for weight reduction especially in transportation industry. A special feature of magnesium solidification is the anisotropy of the hcp lattice. Under directional growth conditions,

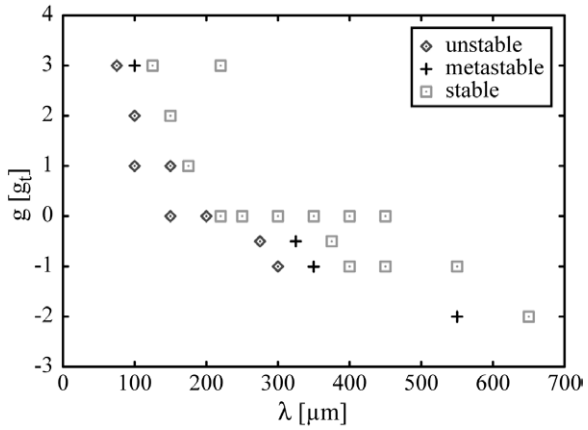

Figure 8. Stability diagram of spacings for different levels of gravity. Reproduced from [82].

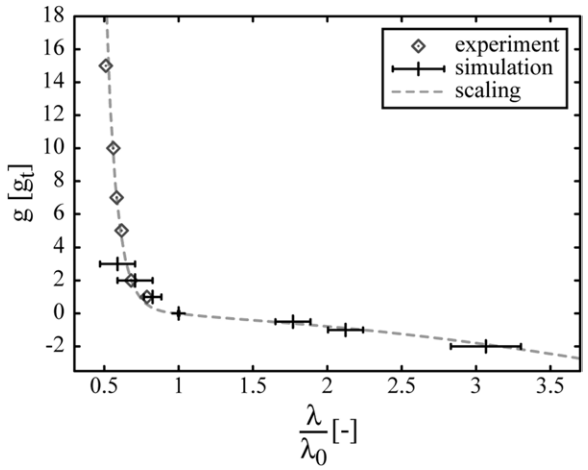

Figure 9. Comparison between experiment, simulation and scaling of the spacing λ, normalized by the spacing λ_0 at gravity $g = 0$. Reproduced with permission from [82], © Elsevier 2009.

a crystallographic texture, which first evolves during growth and is further affected by deformation and recrystallization, is observed. Experimental studies for Mg-alloys state growth along $\langle 1\,1\,2\,0\rangle$ [83, 84] while growth in the basal $\langle 0\,0\,0\,1\rangle$ orientations is suppressed. For phase-field simulation of this growth, a corresponding anisotropy function must first be constructed. This is done in [85] using molecular dynamics data from Xia *et al* [86] and Sun *et al* [87]. As consequence, the grain arrangement is plate-like, situated within the basal plane. Competitive growth is simulated starting from fifty initial seeds with random orientation. Figure 10 shows the dendritic structure after 9s of growth and a comparison between initial and selected orientations. Grains with significant contribution of the basal orientation $\langle 0\,0\,0\,1\rangle$ in gradient direction immediately become overgrown. From the remaining seventeen grains with basal orientations almost perpendicular to the growth direction another eight become overgrown during further selection. Six of the prevailing dendrites have $\langle 1\,1\,2\,0\rangle$ orientations closely aligned to temperature gradient. Their secondary arm orientations can be found close to 60°, and the corresponding $\langle 1\,0\,1\,0\rangle$ orientations close to 30°, and the corresponding $\langle 1\,0\,1\,0\rangle$

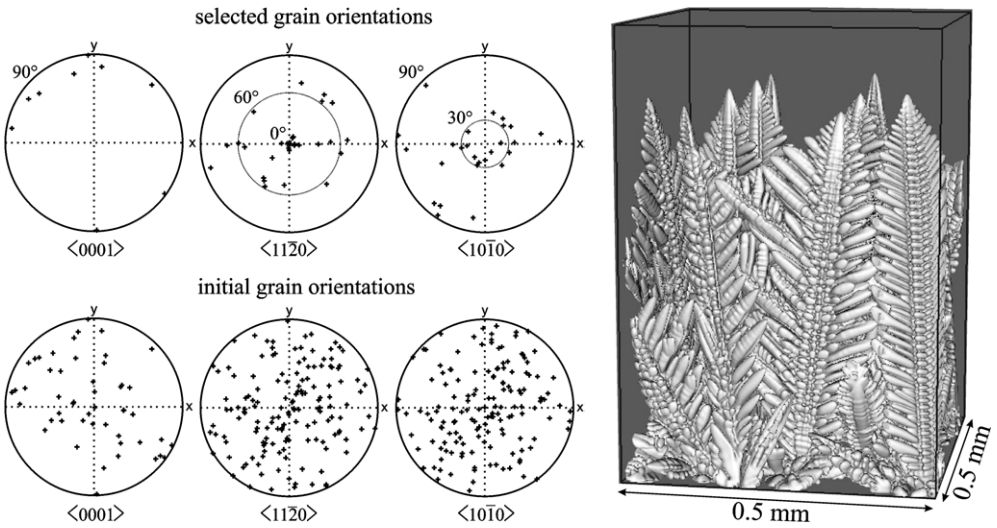

Figure 10. 3D simulation of directional dendritic growth of a Mg–Al alloy. The pole figures show the growth orientation as initially chosen randomly for seeding at the bottom of the domain and after orientation selection by growth. Reproduced with permission from [85] (Maney Publishing).

orientations close to 30° and 90° misorientation. Three dendrites with distinctly misaligned ⟨1 1 2 0⟩ orientation remain. As all grains grow with almost plate-like geometry, interaction is already reduced in this stage and the prevailing grains may eventually stably coexist during further growth.

4.5. Multicomponent dendrites

Another step in the direction of simulation of phase transformation in technical materials and processes is the consideration of multicomponent multi-phase materials and of metastability by suppressed nucleation of stable phases. This can only be done by direct coupling to thermodynamic databases and by augmenting the deterministic phase-field and transport equations by statistical models of nucleation. The first coupling of a phase field to a thermodynamic database was published by Grafe *et al* [88] and others followed [28, 89–94]. The level of sophistication ranges from extracting the expansion parameters of the chemical free energy function from a CALPHAD database to online coupling between phase-field calculation of interface movement and CALPHAD quasi-equilibrium calculation as realized in the MICRESS code [54, 37]. Nucleation has to be taken into account for prediction of grain sizes. Noise can be added to the phase-field equation to overcome the nucleation barrier in a first order phase transition (see [95] for a review). In a phase-field simulation on a micrometer scale, however, only large critical nucleation sizes can be resolved with an unrealistic amplitude of the fluctuation. Therefore statistical models based on a prescribed size distribution of inoculant particles are used here [96, 97].

Figure 11 shows a qualitative comparison between the simulated and experimental microstructure of the typical hypereutectic four component AlCuSiMg piston alloy (reproduced from [98]). The homogenous melt is cooled with a constant heat extraction rate. A seed density model has been applied for nucleation of primary silicon particles. During growth of the primary silicon, the melt is depleted from silicon. Reaching the eutectic composition one would expect that solidification terminates in an eutectic mode. However, since the crystal

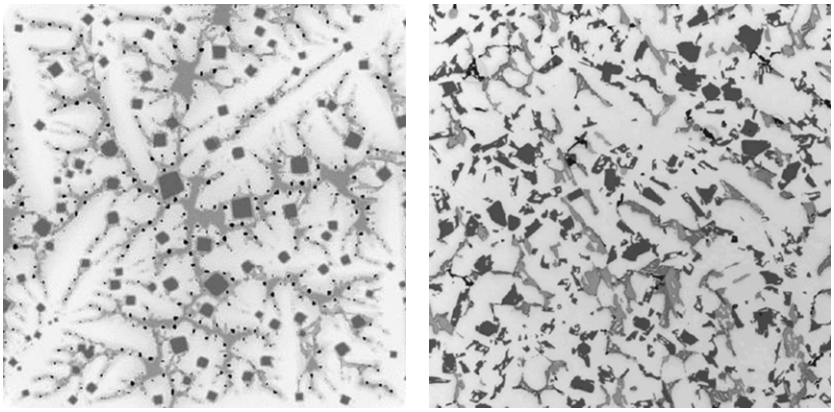

Figure 11. Comparison between simulation (left) and experiment (right) for KS1295. The area is 400 μm × 400 μm in both images. However the exact temperature history in the experiment and good values for the different nucleation barriers are not known accurately for a quantitative comparison. Reproduced with permission from [98], © Elsevier 2006.

lattices of silicon and the fcc-Al phase are quite different, nucleation of the fcc-Al phase on the silicon particles requires a very high undercooling and therefore was disabled in the simulation. Instead, it is assumed that fcc-Al would nucleate heterogeneously on seed particles in the melt with an assumed undercooling of 2K. Fcc-Al phase then starts to grow in a dendritic manner. Nucleation of Mg_2Si (black particles in figure 11) has been included in the simulation with a nucleation undercooling of 5 K on the fcc-Al surface. However, this phase becomes thermodynamically stable only well below the Al–Si eutectic temperature. Using the given assumptions on nucleation the sequence of solid phases: primary silicon-fcc-Al—secondary silicon—Mg_2Si can be reproduced in accordance with the experimental observation, indicating a pronounced non-equilibrium solidification path.

4.6. Pearlitic transformation in FeC

The pioneering work of Zener and Hillert in the 1950s [99, 100] on the cooperative growth mode of pearlite can be viewed as the first transformation model in materials science where the connection of transformation kinetics and structure was demonstrated. The model explains diffusion of carbon in austenite ahead of the ferrite and cementite lamellae as the rate controlling process for the transformation. The time needed for diffusion is thus connected to the lamellar spacing. A fine spacing would be preferential for a fast transient to equilibrium. Such a fine spacing, however, implies the creation of a high amount of interfaces, which hinders the transformation. Thereby an optimal spacing can be defined. It was shown that the model explains quantitatively experimental observation of eutectic solidification [101] while it fails to predict the observed growth kinetics in the eutectoid solid state transformation of pearlite accurately [102–104]. This is because of the neglect of diffusion in the parent phases as well as the neglect of stress and strain effects, which are important in solid state. The consideration of these effects in an analytical treatment is difficult whereas they can be treated consistently in a phase-field model. Here, in particular, the phase-field model can employ its full power because the growth structure does not need to be prescribed but is a result of the calculation. It was recently possible to resolve the discrepancy between experimental observations and the model prediction by applying the MPF model coupled to transformation strain, strain due

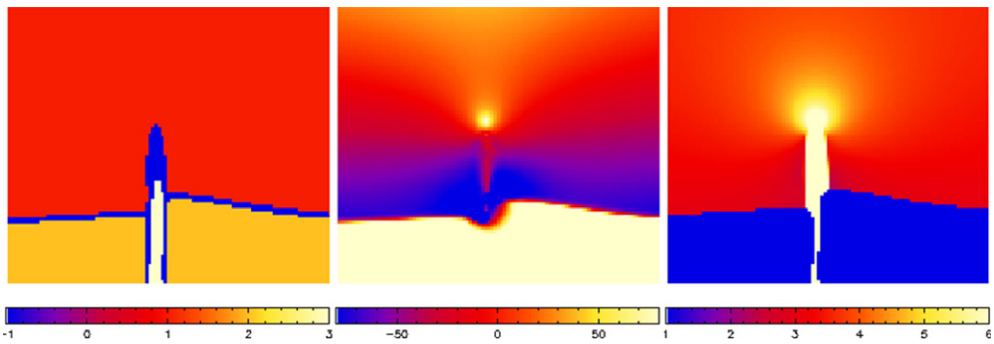

Figure 12. Snapshot of the tip region as calculated for the staggered growth mode. Left: Phase distribution. Middle: Hydrostatic stress in (MPa). The austenite around the cementite tip is under large expansion, caused by the lattice match to cementite. A large part of the expansion is compensated by enrichment of carbon. Therefore elastic stress is limited to 90 MPa. Right: Carbon distribution around the cementite tip in (at%). The carbon enrichment is mainly due to the expansion of the austenite lattice. The concentration reaches its maximum at 6 at% in austenite. Reproduced with permission from [57], © Elsevier 2007.

to concentration gradients and stress driven diffusion [57, 105]. Furthermore, a new growth mode, staggered growth, was predicted where cementite needles grow ahead of the ferrite front and where the expansion of cementite causes a dilatation of the austenite lattice that has to be compensated by uphill diffusion of carbon to the cementite tip. The calculated structure of the transformation front together with stress and carbon concentration distribution close to steady state is depicted in figure 12. The coupled phase field, diffusion and stress calculation is computationally very demanding. In particular the coupling between stress and diffusion tends to oscillating modes and destabilizes the calculations. Therefore only one cementite lamella could be calculated in a periodical arrangement. However the calculations provide clear evidence of the existence of the staggered growth mode and predict transformation kinetics in the experimentally observed regime. Additional effects such as faceting of the interfaces, partial coherency and the effect of other alloying elements are subject to further investigation.

4.7. Rafting in single crystal Ni-base superalloys

Another example of successfully applying the phase-field method to gain fundamental understanding of microstructural evolution in complex alloy systems is the recent work on quantitative computer modeling of γ' rafting (directional coarsening) and the corresponding creep deformation in Ni-base superalloys [106–109]. Three-dimensional phase-field simulations of coupled γ/γ' microstructural evolution and plastic deformation were carried out at two different length scales. For the first time, the relative contributions from modulus mismatch, channel plasticity and the combination of the two to γ' rafting have been discriminated by dislocation-level simulations [106, 107] (figure 13). Quantitative comparisons of times to reach complete rafting, driving force variations and microstructural evolution during rafting among these cases showed that channel plasticity played the dominant role in controlling the rafting process. Based on this finding, micrometer-scale simulations [108, 109] that take into account plastic deformation in γ-channels, described by local channel dislocation densities from individual active slip systems, were carried out. The rafting kinetics, precipitate-matrix inversion process and the corresponding creep deformation were characterized at different values of applied stress, lattice misfit and precipitate volume fraction

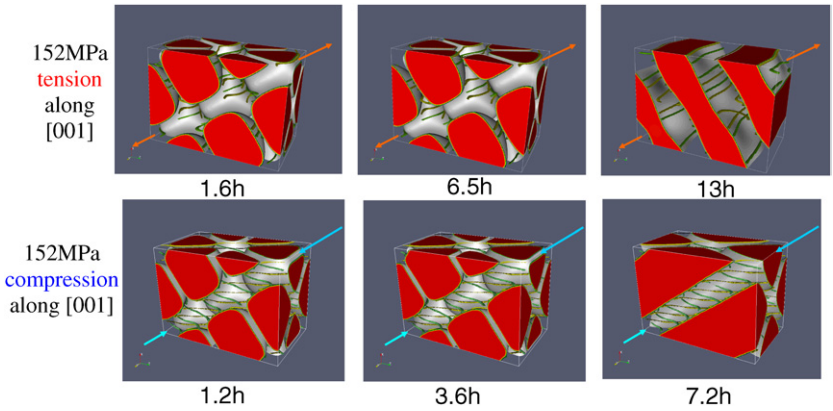

Figure 13. Dislocation-level phase-field simulations of coupled γ/γ' microstructural evolution and dislocation activities in γ-channel. Two slip systems were considered (i.e. $\frac{1}{2}[1\,0\,1](-1\,-1\,1)$ and $\frac{1}{2}[0\,1\,1](-1\,-1\,1)$) and the lattice misfit between the γ and γ' phases is -0.3%. For more details see [108].

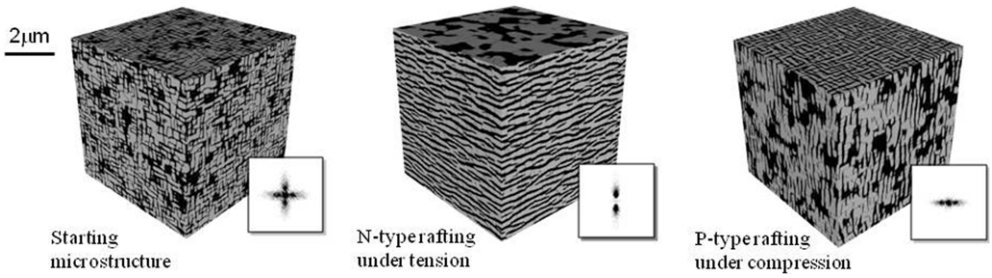

Figure 14. Large-scale phase-field simulation of rafting in Ni–Al. The simulation results were obtained after 9 h aging at 1300 K with uniformly distributed dislocation the γ-channel of 100 nm spacing. The lattice misfit of the alloy is -0.3%. For more details see [109].

(figure 14). The simulation results were compared with experiments carried out for Ni–Al–Cr [110]. Quantitative agreement was obtained. With the assistance of these models, the interplay between elastic inhomogeneity and channel plasticity can be characterized and utilized to offer opportunities for possible new design strategies to improve control of the rafting process.

4.8. Ferroelectric phase transitions in $BaTiO_3$

Another exiting application of phase-field modeling in materials science is transitions where structural degrees of freedom are closely linked to electrical degrees of freedom, as in ferroelectric materials. In this case, another energy contribution has to be added to the phase-field free energy functional, the electric free energy f^{elec} with the electric field $\vec{E}$ and the polarization direction $\vec{e_\alpha}$ of the variant α.

$$f^{\text{elec}} = \sum_{\alpha=1,..,N} \vec{E}\vec{e}_\alpha \phi_\alpha. \tag{54}$$

Phase transitions in $BaTiO_3$, grown epitaxially on a substrate, involve not only spontaneous polarization, but also dilatation of lattice parameters. The amount of shifts will depend on

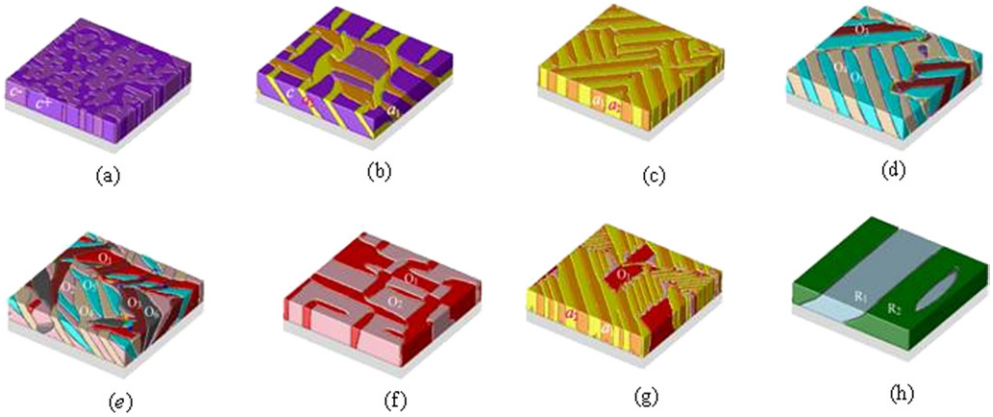

Figure 15. Representative domain morphologies in $BaTiO_3$ films within different domain stability fields. (*a*) at $T = 25\,^{\circ}$C and $= -1.0\%$ strain; (*b*) at $T = 75\,^{\circ}$C and $= 0.0\%$ strain; (*c*) at $T = 50\,^{\circ}C$ and $= 0.2\%$ strain; (*d*) at $T = -25\,^{\circ}$C and $= -0.05\%$ strain; (*e*) at $T = -25\,^{\circ}$ C and $= 0.1\%$ strain; (*f*) at $T = 25\,^{\circ}$C and $= 1.0\%$ strain; (*g*) at $T = 25\,^{\circ}$C and $= 0.25\%$ strain; (*h*) at $T = -100\,^{\circ}$C and $= 0.1\%$ strain. Reproduced with permission from [19]. © 2006 American Institute of Physics.

the film orientation, the degree of coherency between film and substrate, temperature, strain magnitude and anisotropy. For the particular case of (0 0 1)-oriented $BaTiO_3$ film under a symmetrical biaxial constraint, the phase transition temperatures and domain stabilities as a function of strain have been obtained using phase-field simulations [20]. All the simulations started from a homogeneous paraelectric state with small random noise of uniform distribution. Examples of domain structures from the simulations are shown in figure 15, reproduced from [20]. Under sufficiently large compressive strains ($>-0.8\%$), there is only one ferroelectric transition, and the rest disappears. The ferroelectric phase is of tetragonal symmetry (T^{P}) with polarization directions orthogonal to the film/substrate interface. Figure 15(*a*) is a typical domain structure under large compressive strains, in which there are two types of c-domains (c+ and c−) separated by 180° domain walls. On the tensile side, there are only two ferroelectric phase transitions for strain values greater than +0.6%. The polarization directions for the two ferroelectric phases are parallel to the film/substrate interface, either along [1 0 0] (O_1^{f}) or [1 1 0] (O_2^{f}) direction, depending on temperature and the magnitude of strain. The corresponding domain structures are similar to either the a1/a2 twins as shown in figure 15(*c*), or the orthorhombic twins of figure 15(*f*), or the mixture of them shown in figure 15(*g*). Under relative smaller strains, the ferroelectric phase transitions and domain structures of various ferroelectric phases are similar to bulk single crystals. At room temperature, the domain structures vary from pure c-domains to c/a1/a2 then to a1/a2 twins, a mixture of a1/a2 and O1/O2 twins, and O1/O2 twins when the substrate constraint changes from compressive to tensile. It is known that there are also other regions in which more than two or more ferroelectric phases coexist.

5. Conclusion

The phase-field method provides a tool for the simulation of microstructure evolution in complex materials on the mesoscopic scale. It is based on the thermodynamic description of non-equilibrium states in materials including interfaces. The phase field is formulated as a state variable in space and time, the evolution of which controls the pathway towards

equilibrium. Dynamical equations are derived from the principle of entropy maximization applying relaxational dynamics. The thin interface limit with kinetic and anti-trapping correction for solutal transformations guarantees a maximum of numerical efficiency by reducing numerical artifacts due to the diffusivity of the interface region beyond the atomistic scale of a real interface. Furthermore the MPF method provides a flexible framework to include transitions between multiple phases in multicomponent materials. Different modes of transport like diffusion and advection can be treated as well as mechanical, electrical and magnetic interactions. The examples presented only illustrate a small part of the various possible applications of the method. They clearly demonstrate that today phase-field simulations are ready to solve practical problems in materials science.

Appendix A

A.1. Traveling wave solution for the double well potential

We will start from the phase-field equation in the Kobayashi's notation equation (1) in one-dimensional form and the corresponding functional. The temperature will be treated as constant.

$$\tau_{\mathrm{DW}}\dot{\phi} = \epsilon_{\mathrm{DW}}\frac{\partial^2}{\partial x^2}\phi - \gamma_{\mathrm{DW}}\phi(1-\phi)\left(\phi - \tfrac{1}{2}\right) + m_{\mathrm{DW}}\phi(1-\phi), \tag{55}$$

$$F = \int_\Omega \mathrm{d}x \left\{\frac{1}{2}\epsilon_{\mathrm{DW}}|\nabla\phi|^2 + \frac{\gamma_{\mathrm{DW}}}{4}\phi^2(1-\phi)^2 - m_{\mathrm{DW}}\left(\frac{\phi^2}{2} - \frac{\phi^3}{3}\right)\right\}. \tag{56}$$

The thermodynamic driving force $m_{\mathrm{DW}}((\phi^2/2) - (\phi^3/3))$ is directly related to the Gibbs free energy difference $\Delta g = g(\phi = 1) - g(\phi = 0)$ between the bulk phases and fixes the energy scale

$$m_{\mathrm{DW}} = -6\Delta g. \tag{57}$$

The steady state solution of (55) has the form of a hyperbolic tangent profile of width η marking the transition zone between 5% and 95% traveling with constant speed v_n

$$\phi(x,t) = \frac{1}{2}\tanh\left(\frac{3(x - v_n t)}{\eta}\right) + \frac{1}{2} \tag{58}$$

To prove the validity of the solution we just have to compute the derivatives

$$\frac{\partial\phi}{\partial x} = \frac{6}{\eta}\phi(1-\phi), \tag{59}$$

$$\frac{\partial^2\phi}{\partial x^2} = \frac{72}{\eta^2}\phi(1-\phi)\left(\frac{1}{2} - \phi\right). \tag{60}$$

Inserting (59) and (60) into (55) we have

$$\begin{aligned}\tau_{\mathrm{DW}}\dot{\phi} = & -\tau_{\mathrm{DW}}v_n\frac{\partial\phi}{\partial x} = -v_n\frac{6\tau_{\mathrm{DW}}}{\eta}\phi(1-\phi)\\ = & \left(\epsilon_{\mathrm{DW}}\frac{72}{\eta^2} - \gamma_{\mathrm{DW}}\right)\phi(1-\phi)\left(\phi - \frac{1}{2}\right) + m_{\mathrm{DW}}\phi(1-\phi).\end{aligned} \tag{61}$$

Equation (61) becomes independent of ϕ if the term $\epsilon_{\mathrm{DW}}\frac{72}{\eta^2} - \gamma_{\mathrm{DW}}$ vanishes and we have

$$v_n = \frac{-\eta}{6\tau_{\mathrm{DW}}}m_{\mathrm{DW}} = \frac{\eta}{\tau_{\mathrm{DW}}}\Delta g; \qquad \eta = \sqrt{\frac{72\epsilon_{\mathrm{DW}}}{\gamma_{\mathrm{DW}}}}. \tag{62}$$

With the interface mobility μ as the proportionality constant between velocity and driving force Δg the time scale becomes $\tau_{\mathrm{DW}} = \eta/\mu$. The fixation of the length scale η follows from the definition of the interfacial energy. At equilibrium $\Delta g = 0$ the only energy contribution in the system is the interfacial energy per unit area σ

$$\begin{aligned}\sigma &= \int_{-\infty}^{\infty} \mathrm{d}x \left[\frac{\epsilon_{\mathrm{DW}}}{2}(\nabla\phi)^2 + \frac{\gamma_{\mathrm{DW}}}{4}\phi^2(1-\phi)^2\right] \\ &= \int_0^1 \mathrm{d}\phi \left[\frac{\mathrm{d}x}{\mathrm{d}\phi}\left(\frac{18\epsilon_{\mathrm{DW}}}{\eta^2} + \frac{18\epsilon_{\mathrm{DW}}}{\eta^2}\right)\phi^2(1-\phi)^2\right] \\ &= \int_0^1 \mathrm{d}\phi \frac{6\epsilon_{\mathrm{DW}}}{\eta}\phi(1-\phi) = \frac{\epsilon_{\mathrm{DW}}}{\eta} = \frac{\eta\gamma_{\mathrm{DW}}}{72}. \end{aligned} \tag{63}$$

It must also be borne in mind that both the gradient term proportional to ϵ_{DW} and the potential term proportional to γ_{DW} contribute to equal parts to the interfacial energy. This is the equivalent of the law of equal partitioning of kinetic and potential energy in a stationary mechanical system. Summarizing, we find the relations between the model parameters and the physical parameters that are valid close to the steady state solution

$$\epsilon_{\mathrm{DW}} = \sigma\eta, \qquad \gamma_{\mathrm{DW}} = 72\frac{\sigma}{\eta}, \qquad m_{\mathrm{DW}} = -6\Delta g, \qquad \tau_{\mathrm{DW}} = \frac{\eta}{\mu}.$$

A.2. Traveling wave solution for the double obstacle potential

The double obstacle potential is defined as

$$f_{\mathrm{DO}} = \begin{cases} \dfrac{\gamma_{\mathrm{DO}}}{2}\phi(1-\phi) - m_{\mathrm{DO}}h_{\mathrm{DO}}(\phi) & \text{for } 0 \leqslant \phi \leqslant 1, \\ \infty & \text{else,} \end{cases}$$

$$h_{\mathrm{DO}}(\phi) = \tfrac{1}{4}\left[(2\phi-1)\sqrt{\phi(1-\phi)} + \tfrac{1}{2}\arcsin(2\phi-1)\right]. \tag{64}$$

Since $\phi(1-\phi)$ is unbounded to $-\infty$ for the unphysical states $\phi < 0$ and $\phi > 1$ the obstacle $f_{\mathrm{DO}} = \infty$ for these states is introduced [8]. The advantage of the double obstacle potential is the finite slope of the potential at the minima which guarantees the convergence of the phase-field contour to the limiting values 0 and 1 within a finite region of width η. The disadvantage of the potential is the discontinuity of the potential at the edges of the interface. For practical applications, the advantages clearly prevail. The special form of $h_{\mathrm{DO}}(\phi)$ is dictated by the demand that a steady state traveling wave solution independent of the velocity exists. Repeating the analysis as for the double well potential we find

$$F = \int_\Omega \mathrm{d}x \left\{\frac{1}{2}\epsilon_{\mathrm{DO}}|\nabla\phi|^2 + f_{\mathrm{DO}}\right\}. \tag{65}$$

$$\tau_{\mathrm{DO}}\dot{\phi} = \epsilon_{\mathrm{DO}}\nabla^2\phi + \gamma_{\mathrm{DO}}\left(\phi - \tfrac{1}{2}\right) + \sqrt{\phi(1-\phi)}m_{\mathrm{DO}}. \tag{66}$$

$$\phi(x,t) = \begin{cases} 1 & \text{for } x < v_n t - \dfrac{\eta}{2}, \\ \dfrac{1}{2} - \dfrac{1}{2}\sin\left(\dfrac{\pi}{\eta}(x - v_n t)\right), & \text{for } v_n t - \dfrac{\eta}{2} \leqslant x < v_n t + \dfrac{\eta}{2}, \\ 0 & \text{for } x \geqslant v_n t + \dfrac{\eta}{2}. \end{cases} \tag{67}$$

[8] An alternative way to formulate the potential is to use the absolute $\tilde{f}_{\mathrm{DO}} = \frac{\gamma_{\mathrm{DO}}}{2}|\phi(1-\phi)|$ which reflects unphysical states back to the physical range.

$$\frac{\partial}{\partial x}\phi = \frac{\pi}{\eta}\sqrt{\phi(1-\phi)}, \tag{68}$$

$$\frac{\partial^2}{\partial x^2}\phi = \frac{\pi^2}{\eta^2}\left(\frac{1}{2}-\phi\right), \tag{69}$$

$$\epsilon_{\mathrm{DO}} = \frac{8\sigma\eta}{\pi^2}, \qquad \gamma_{\mathrm{DO}} = 8\frac{\sigma}{\eta}, \qquad m_{\mathrm{DO}} = \frac{-8}{\pi}\Delta g, \qquad \tau_{\mathrm{DO}} = \frac{8\eta}{\pi^2\mu}. \tag{70}$$

A.3. Traveling wave solution for the top hat potential

The weighting functions $h(\phi)$ for the double well and double obstacle potentials were constructed such that a traveling wave solution exists, i.e. that the steady state contour does not deform for a moving interface. In general, however, other forms of the function $h(\phi)$ are possible. These only have to satisfy the requirement that the front, as an average, moves with constant velocity as given by the Gibbs–Thomson relation. The moving interface will then deform (in normal direction) dependent on the relation of the driving force Δg to the interfacial energy density σ/η. This deformation can be kept small by adjusting the interface width η and therefore the deformation of the front can be controlled even if other monotonous functions of $h(\phi)$ are used for numerical efficiency. For thermodynamic consistency at the triple junction it is now indispensable to use the unity $h(\phi) = \phi$ (see section 3.4) in a MPF model. It is easy to construct an appropriate potential knowing that $\nabla\phi$ and $\dot{\phi}$ have to be constant in the interface if the (local) driving force is constant. This can be achieved by the use of the top hat potential

$$f_{\mathrm{TH}} = \gamma_{\mathrm{TH}}[\Theta(\phi) - \Theta(\phi-1)] - \phi m_{\mathrm{TH}}, \tag{71}$$

Θ is the stepfunction $\Theta(\phi) = 0$ for $\phi < 0$; $\Theta(\phi) = 1$ for $\phi \geqslant 0$. For completeness an obstacle to cut off against unphysical values of $\phi < 0$ and $\phi > 1$ has to be added which is omitted here for readability.

The phase-field equation now reads

$$\tau_{\mathrm{TH}}\dot{\phi} = \epsilon_{\mathrm{TH}}\nabla^2\phi - \gamma_{\mathrm{TH}}[\delta_{\mathrm{D}}(\phi) - \delta_{\mathrm{D}}(1-\phi)] + m_{\mathrm{TH}} \tag{72}$$

with the piece-wise linear profile as the obvious solution

$$\phi(x,t) = \begin{cases} 1 & \text{for } x < v_n t - \dfrac{\eta}{2}, \\ \dfrac{1}{2} - \dfrac{x - v_n t}{\eta} & \text{for } v_n t - \dfrac{\eta}{2} \leqslant x < v_n t + \dfrac{\eta}{2}, \\ 0 & \text{for } x \leqslant v_n t + \dfrac{\eta}{2}. \end{cases}$$

δ_{D} is the Dirac or delta function as the derivative of the step function Θ. It generates the deflection in the front profile at the edges of the interface. The Laplacian at the edges can be evaluated from a contour smoothened over a distance h in the limit $h \to 0$ (which is demonstrated here for the edge $\phi = 0$ at $x = 0$ only). For smoothing we may use a parabola that has the slope $-1/\eta$ at $x = -h$

$$\phi(x,t) = \frac{x^2}{2\eta h} \quad \text{for} \quad -h < x < 0 \tag{73}$$

$$\lim_{h\to 0}\frac{\mathrm{d}^2\phi}{\mathrm{d}x^2} = \lim_{h\to 0}\frac{1}{h\eta} = \frac{1}{2\eta^2}\delta_{\mathrm{D}}(\phi), \tag{74}$$

where I have substituted $h = 2\eta\phi_{\mathrm{l}}$ at the left boundary of the smoothing area and used the definition of the δ_{D} function: $\delta_{\mathrm{D}}(\phi) = \lim_{\phi_{\mathrm{l}}\to 0}(1/\phi_{\mathrm{l}})$ for $0 < \phi < \phi_{\mathrm{l}}$ and 0 elsewhere. The relations between the model parameters and the physical parameters read

$$\epsilon_{\mathrm{TH}} = \sigma\eta, \qquad \gamma_{\mathrm{TH}} = \frac{\sigma}{2\eta}, \qquad m_{\mathrm{TH}} = -\Delta g, \qquad \tau_{\mathrm{TH}} = \frac{\eta}{\mu}.$$

I am not aware that this potential is ever used in a numerical simulation. The singularity at the edges of the interface can be assumed to cause a large discretization dependence, the avoidance of which ins one central goal of any numerical scheme. However, it might be useful for the investigation of thermodynamically driven triple junction motion.

Acknowledgments

The author would like to thank the German Research Foundation (DFG) for financial support under the integrated project SPP1120, grant number STE1116/1 and under SPP1268, grant number STE1116/4. The permission to reproduce results from Ryo Kobayashi, Seon Geon Kim, Alain Karma, Bernd Böttger, Janin Eiken, Yunzhi Wang, Long-Quing Chen is highly appreciated. Finally I thank Robert Spatschek and Wei Guo for crossreading the manuscript and helpful comments.

References

[1] Karma A 2001 Phase-field formulation for quantitative modeling of alloy solidification *Phys. Rev. Lett.* **87** 115701
[2] Karma A 2001 Phase-field methods *Encyclopedia of Materials Science and Technology* ed K H J Buschow *et al* (Oxford, UK: Elsevier) pp 6873–86
[3] Boettinger W J, Warren J A, Beckermann C and Karma A 2002 Phase-field simulation of solidification *Annu. Rev. Mater. Res.* **32** 163–94
[4] Chen L-Q 2002 Phase-field models for microstructure evolution *Annu. Rev. Mater. Res.* **32** 113–40
[5] Thornton K, Agren J and Voorhees P W 2003 Modelling the evolution of phase boundaries in solids at the meso- and nano-scales *Acta Mater.* **51** 5675–710
[6] Moelans N, Blanpain B and Wollants P 2008 An introduction to phase-field modeling of microstructure evolution *Comput. Coupling Phase Diagr. Thermochem.* **32** 268–94
[7] Kitashima T 2008 Coupling of the phase-field and CALPHAD methods for predicting multicomponent, solid state phase transformations *Phil. Mag.* **88** 1615–37
[8] Rowlinson J S 1979 Translation of J D van der Waals 'The thermodynamik theory of capillarity under the hypothesis of a continuous variation of density' *J. Stat. Phys.* **20** 197–200
[9] Landau L D and Khalatikow I M 1963 *The Selected Works of L.D. Landau* (Engl. transl.) (Oxford: Pergamon)
[10] Hillert M 1956 A theory of nucleation for solid solutions *D.Sc Thesis* (Cambridge, MA: MIT Press)
[11] Cahn J E and Hilliard J E 1958 Free energy of a nonuniform system: I. Interfacial free energy *J. Chem. Phys.* **28** 258–67
[12] Cahn J E and Hilliard J E 1959 Free energy of a nonuniform system: III. Nucleation in a two-component incompressible fluid *J. Chem. Phys.* **31** 688–99
[13] Langer J S 1987 *Chance and Matter, Lectures on the theory of pattern formation Les Houches, session XLVI (Amsterdam, The Netherlands)* ed J Souletie *et al* pp 692–711
[14] Khachaturyan A G 1983 *Theory of Structural Transformations in Solids* (New York: Wiley)
[15] Wang Y, Chen L-Q and Khachaturyan A 1994 Computer simulation of microstructure evolution in coherent solids *Solid→Solid Phase Transformations* ed W C Howe *et al* (Warrendale, PA: TMMS) pp 245–65
[16] Wang Y, Chen L-Q and Khachaturyan A 1995 Modeling of dynamical evolution of micro/mesoscopic morphological patterns in coherent phase *Computer Simulation in Materials Science-nano/meso/macroscopic Space and Time Scales* (*Nato ASI Series*) eds H O Kirchner, L Kubin and V Pontikis (Dordrecht: Kluwer)
[17] Wang Y U, Jin Y M, Cuitino A M and Khachaturyan A G 2001 Nanoscale phase field microelasticity theory of dislocations: model and 3d simulations *Acta Mater.* **49** 1947–857
[18] Wang Y and Khachaturyan A G 2006 Multi-scale phase field approach to martensitic transformation *Mater. Sci. Eng.* A **438–440** 55–63
[19] Li L Y and Chen L Q 2006 Temperature–strain phase diagram for $BaTiO_3$ thin films *Appl. Phys. Lett.* **88** 072905
[20] Chen L-Q 2008 Phase-field method of phase transitions/domain structures in ferroelectric thin films: a review *J. Am. Ceram. Soc.* **91** 1835–44
[21] Boettinger W J, Wheeler A A, Murray B T, McFadden G B and Kobayashi R 1993 Calculation of alloy solidification morphologies using the phase-field method *Modeling of Casting, Welding and Advanced Solidification Processes VI* ed T S Pivonka *et al* (Warrendale, PA: TMMS) 79–86

[22] Kobayashi R 1993 Modelling and numerical simulations of dendritic crystal growth *Physica D* **63** 410–23
[23] Kobayashi R 1994 A numerical approach to three-dimensional dendritic solidification *Exp. Math.* **3** 59–81
[24] Onsager L 1931 Reciprocal relations in irreversible processes *Phys. Rev.* **37** 405
[25] Wang S-L, Sekerka R F, Wheeler A A, Murray B T, Coriell S R, Rraun R J and McFadden G B 1993 Thermodynamically-consistent phase-field models for solidification *Physica D* **69** 189–200
[26] Collins J B and Levine H 1985 Diffuse interface model of diffusion-limited crystal growth *Phys. Rev.* B **31** 6119–22
[27] Caginalp G and Fife P 1986 Phase-field methods for interfacial boundaries *Phys. Rev.* B **33** 7792–4
[28] Wu K, Chang Y A and Wang Y 2004 Simulating interdiffusion microstructures in Ni–Al–Cr diffusion couples: a phase field approach coupled with calphad database *Scr. Mater.* **50** 1145–50
[29] Tiaden J, Nestler B, Diepers H J and Steinbach I 1998 The multiphase-field model with an integrated concept for modeling solute diffusion *Physica D* **115** 73–86
[30] Kim S G, Kim W T and Suzuki T 1999 Phase-field model for binary alloys *Phys. Rev.* E **60** 7186–97
[31] Warren J A and Boettinger W J 1995 Prediction of dendritc growth and microsegregation patterns in a binary alloy using the phase-field method *Acta Metall. Mater.* **43** 689–703
[32] Wheeler A A, Boettinger W J and McFadden G B 1993 Phase-field model of solute trapping during solidification *Phys. Rev.* E **47** 1893–909
[33] Ahmad N A, Wheeler A A, Boettinger W J, McFadden G B 1998 Solute trapping and solute drag in a phase-field model of rapid solidification *Phys. Rev.* E **58** 3436–50
[34] McFadden J B, Wheeler A A, Braun R J and Coriell S R 1993 Phase-field models for anisotropic interfaces *Phys. Rev.* E **48** 2016–24
[35] Wheeler A A 1999 Cahn-hoffman xi-vector and its relation to diffusi interface models of solidification *J. Stat. Phys.* **95** 1245–80
[36] Caginalp G 1989 Stefan and hele-shaw type models as asymptotic limits of the phase-field equation *Phys. Rev.* A **39** 5887–96
[37] Eiken J, Böttger B and Steinbach I 2006 Multi phase field approach for alloy solidification *Phys. Rev.* E **73** 066122
[38] Steinbach I and Apel M 2007 Phase-field simulation of rapid crystallization of silicon on substrate *Mater. Sci. Eng.* A **449** 95–8
[39] Herring C 1952 The use of classical macroscopic concepts in surface-energy problems *Structure and Properties of Solid Surfaces* ed R Gomer and C S Smith (Chicago: University of Chicago Press)
[40] Karma A and Rappel W-J 1996 Phase-field method for computational efficient modeling of solidification with arbitrary interface kinetics *Phys. Rev.* E **53** 3017–20
[41] Karma A and Rappel W-J 1998 Quantitative phase-field modelling of dendritic growth in two and three dimensions *Phys. Rev.* E **57** 4323–49
[42] Echebarria B, Folch R, Karma A and Plapp M 2004 Quantitative phase-field model of alloy solidification *Phys. Rev.* E **73** 061604
[43] Ramirez J C, Beckermann C, Karma A and Diepers H-J 2004 Phase-field modelling of binary alloy solidification with coulpled heat and solute diffusion *Phys. Rev.* E **69** 051607–22
[44] Kim S G 2007 A phase-field model with antitrapping current for multicomponent alloys with arbitrary thermodynamic properties *Acta Mater.* **55** 4391–99
[45] Pariser G, Schaffnit P, Steinbach I and Bleck W 2001 Simulation of γ–α transformation using the phase-field method *Steel Res.* **72** 354–60
[46] Karma A 1994 Phase-field model of eutectic growth for computational *Phys. Rev.* E **49** 2245–9
[47] Wheeler A A, Boettinger W J and McFadden G B 1996 Phase-field model for solidification of a eutectic alloy *Proc. R. Soc. Lond. Ser. A—Math. Phys. Eng. Sci.* **452** 495–525
[48] Steinbach I, Pezzolla F, Nestler B, Seeßelberg M, Prieler R, Schmitz G J and Rezende J L L 1996 A phase field concept for multiphase systems *Physica D* **94** 135–47
[49] Steinbach I and Pezzolla F 1999 A generalized field method for multiphase transformations using interface fields *Physica D* **134** 385–93
[50] Steinbach I and Apel M 2006 Multi phase field model for solid state transformation with elastic strain *Physica D* **217** 153–60
[51] Fan D N and Chen L Q 1996 Microstructural evolution and grain growth kinetics in two -phase silids with auqdrijunctions *Mathematics of Microstructure Evolution* (Warrendale, PA: TMS) pp 215–23
[52] Fan D N and Chen L Q 1997 Computer simulation of grain growth using adiffuse-interface model: Local kinetics and topology *Acta Mater.* **45** 1115–26
[53] Kobayashi R, Warren J A and Carter W C 1998 Mathematical models for solidification and grain boundary formation *Ach-Mod. Chem.* **135** 287–95

[54] www.micress.de
[55] Folch R and Plapp M 2003 Towards a quantitative phase-field model of two-phase solidification *Phys. Rev.* E **68** 010602
[56] Folch R and Plapp M 2005 Quantitative phase-field modeling of two-phase solidification *Phys. Rev.* E **72** 011602
[57] Steinbach I and Apel M 2007 The influence of lattice strain on pearlite formation in Fe–C *Acta Mater.* **55** 4817–22
[58] Beckermann C, Diepers H-J, Steinbach I, Karma A and Tong X 1999 Modeling melt convection in phase-field simulations of solidification *J. Comput. Phys.* **154** 468–96
[59] Diepers H-J, Beckermann C and Steinbach I 1999 Simulation of convection and ripening in a binary alloy mush using the phase-field method *Acta Mater.* **47** 3663–78
[60] Jeong J-H, Goldenfeld N and Dantzig J 2001 Phase field model for three-dimensional dendritic growth with fluid flow *Phys. Rev.* E **64** 041602
[61] Ramirez J C, Lu Y and Beckermann C 2005 Three-dimensional phase-field simulation of the effect of convection on free dendritix growth *J. Cryst. Growth* **280** 320–34
[62] Apel M and Steinbach I 2008 Dendritic solidification in the diffusive regime and under the influence of buoyancy-driven convection *Phase Transformation in Multicompontent Melts* ed D Herlach (New York: Wiley-VCH) pp 373–85
[63] Anderson D M, McFadden G B and Wheeler A A 2000 A phase-field model of solidification with convection *Physica D* **135** 175–94
[64] Anderson D M, McFadden G B and Wheeler A A 2001 A phase-field model of solidification with convection: sharp-interface asymptotics *Physica D* **151** 305–31
[65] Medvedev D, Fischaleck T and Kassner K 2007 Influence of external flows on pattern growth *J. Cryst. Growth* **303** 69–73
[66] Lee Y-W, Smith R N, Glicksman M E and Koss M B 1996 Effect of buoyancy on the growth of dendritic crystals *Annual Review of Heat Transfer* ed C L Tien (New York: Begell House) p 59
[67] Mullins W W and Sekerka R F 1963 Morphological stability of a particle growing by diffusion or heat flow *J. Appl. Phys.* **34** 323
[68] Hoyt J J, Asta M, Haxhimali T, Karma A, Napolitano R E, Trivedi R, Laird B B and Morris J R 2004 *MRS Bull.* **29** 935–9
[69] Ben-Amar M and Brenner E 1993 *Phys. Rev. Lett.* **71** 589
[70] Haxhimali T, Karma A, Gonzales F and Rappaz M 2006 Orientation selection in dendritic evolution *Nature Mater.* **5** 660–4
[71] Hoyt J J, Asta M and Karma A 2001 A method for computing the anisotropy of the solid–liquid interfacial free energy *Phys. Rev. Lett.* **86** 5530–33
[72] Hoyt J J, Asta M and Karma A 2003 Atomistic and continuum modeling of dendritic solidification *Mater. Sci. Eng.* **41** 121–63
[73] Sémoroz A, Durandet Y and Rappaz M 2001 EBSD characterization of dendrite growth directions, texture and misorientations in hot-dipped Al-Zn coatings *Acta. Mater.* **49** 529–41
[74] Allen D J and Hunt J D 1979 *Solidification and Casting of Metals, Proc. Int. Conf. Solidification (Sheffield, 1977)* (*The Metals Society Book 192*) (London: Metals Society) pp 3–9
[75] Kurz W and Fisher D J 1998 *Fundamentals of Solidification* (Zürich: Trans Tech Publications)
[76] Ma D and Sahm P R 1998 Primary spacing in directional solidification *Metall. Mater. Trans.* A **29** 1113–9
[77] Steinbach I 2008 Effect of interface anisotropy on the spacing selection in constraind dendrite growth *Acta Mater.* **56** 4965–71
[78] Ma D 2002 Modeling of primary spacing selection in dendrite arrays during directional solidification *Metall. Mater. Trans.* B **33** 223–33
[79] Diepers H-J, Ma D and Steinbach I 2002 History effects during the selection of primary dendrite spacing. comparison of phase-field simulations with experimental observations *J. Cryst. Growth* **237–239** 149–53
[80] Mathiesen R H and Arnberg L 2005 X-ray radiography observation of columnar dendritic growth and cosnstitutional undercooling in an Al–30wt%Cu alloy *Acta Mater.* **53** 947–56
[81] Battaile C C, Grugel R N, Hmelo A B and Wang T G 1994 The effect of enhanced gravity levels on microstructural development in pb-50 wt pct sn alloys during controlled solidification *Metall. Trans.* A **25** 865–70
[82] Steinbach I 2009 Pattern formation in constraint dendritic growth with solutal buoyancy *Acta Mater.* **57** 2640–5
[83] Pettersen K and Ryum N 1989 *Metall. Trans.* A **20** 847–52
[84] Pettersen K, Lohne O and Ryum N 1990 *Metall. Trans.* A **21** 221–30
[85] Eiken J 2009 Dendritic growth texture evolution in Mg-based alloys investigated by phase-field simulation *Int. J. Cast Met. Res.* at press

[86] Xia Z G, Sun D Y, Asta M and Hoyt J J 2007 *Phys. Rev.* B **75** 012103
[87] Sun D Y, Mendelev M I, Becker C A, Kudin K, Haxhimali T, Asta M, Hoyt J, Karma A and Srolovitz D J 2006 *Phys. Rev.* B **73** 024116
[88] Grafe U, Böttger B, Tiaden J and Fries S G 2000 Coupling of multicomponent thermodynamic databases to a phase field model: Application to solidification and solid state transformations of superalloys *Scr. Mater.* **42** 1179–86
[89] Yeon D-F, Cha P-R and Yoon J-K 2001 A phase-field study for ferrite–austenite transition under para-equilibrium *Scr. Mater.* **45** 661–8
[90] Cha P-R, Yeon D-H and Yoon J-K 2001 A phase field model for isothermal solidification of multicomponent alloys *Acta Mater.* **49** 3295–307
[91] Zhu J Z, Liu Z K, Vaithyanathan V and Chen L Q 2002 Linking phase-field model to calphad: application to precipitate shape evolution in Ni-base alloys *Scr. Mater.* **46** 401–06
[92] Qin R S and Wallach E R 2003 A phase-field model coupled with a thermodynamic database *Acta. Mater.* **51** 6199–210
[93] Kobayashi H, Ode M, Kim S G, Kim W T and Suzuki T 2003 Phase-field model for solidification of ternary alloys coupled with thermodynamic database *Scr. Mater.* **48** 689–94
[94] Chen Q, Ma N, Wu K and Wang Y 2004 Quantitative phase field modeling of diffusion-controlled precipitate growth and dissolution in Ti–Al–V *Scr. Mater.* **50** 471–6
[95] Gránásy L, Pusztai T, Börzsönyi T, Tóth G, Tegze G, Warren J A and Douglas J F 2006 Phase field theory of crystal nucleation and polycrystalline growth: a review *J. Mater. Res.* **21** 309–19
[96] Greer A L, Cooper P S, Meredith M W, Schneider W, Schuhmacher P, Spittle J A and Tronche A 2003 Grain refinement of aluminium alloys by inoculation *Adv. Eng. Mater.* **5** 81–91
[97] Quested T E and Greer A L 2004 The effect or the size distribution of inoculant particles on as-cast grain size in aluminium alloys *Acta Mater.* **52** 3859–68
[98] Böttger B, Eiken J and Steinbach I 2006 Phase field simulation of equiaxed solidification in technical alloys *Acta. Mater.* **54** 2697–704
[99] Zener C 1947 *Kinetics of the Decomposition of Austenite* (New York: Wiley-Interscience)
[100] Hillert M 1957 The role of interfacial energy during solid state phase transformations *Jernkontorets Annaler* **147** 757–89
[101] Jackson K A and Hunt J D 1966 Lamellar and rod eutectic growth *Trans. Metall. Soc. AIME* **236** 1129–42
[102] Brown D and Ridley N 1969 *J. Iron Steel Inst.* **207** 1232–40
[103] Verhoeven J D and Pearson D D 1984 Forced velocity pearlite in high purity Fe–C alloys: II. Theoretical *Metall. Trans.* A **15** 1047–54
[104] Whiting M J 2000 A reaprraisal of kinetic data for the growth of pearlite in high purity Fe–C eutectoid alloys *Scr. Mater.* **43** 969–75
[105] Nakajima K, Apel M and Steinbach I 2006 The role of carbon diffusion in ferrite on the kinetics of cooperative growth of pearlite: a multi-phase field study *Acta Mater.* **54** 3665–72
[106] Zhou N, Shen C, Mills M J and Wang Y 2007 Phase field modeling of channel dislocation activity and γ' rafting in single crystal Ni–Al *Acta Mater.* **55** 5369–81
[107] Zhou N, Shen C, Mills M J and Wang Y 2008 Contributions from elastic inhomogeneity and from plasticity to γ' rafting in single crystal Ni–Al *Acta Mater.* **56** 6156–73
[108] Zhou N, Shen C, Sarosi P M, Mills M J, Pollock T M and Wang Y 2009 γ' rafting in single crystal blade alloys: a simulation study *Mater. Sci. Technol.* **25** 205–12
[109] Zhou N, Shen C, Mills M J and Wang Y Large-scale three-dimensional phase field simulation of γ'-rafting, precipitate-matrix inversion and creep deformation in single crystal superalloys unpublished
[110] Fahrmann M, Hermann W, Fahrmann E, Boegli A and Pollock T 1999 Computer simulation of grain growth using adiffuse-interface model: local kinetics and topology *Mater. Sci. Eng.* A **260** 1115–26